

CELL RHEOLOGY

Mush rather than machine

The cytoplasm of living cells responds to deformation in much the same way as a water-filled sponge does. This behaviour, although intuitive, is connected to long-standing and unsolved fundamental questions in cell mechanics.

Enhua H. Zhou, Fernando D. Martinez and Jeffrey J. Fredberg

We often think of the cell as being an astounding machine. Indeed, the cell has the capabilities to contract, stiffen, stretch, fluidize, reinforce, crawl, intravasate, extravasate, invade, engulf, divide, swell, shrink or remodel. This impressive mechanical repertoire can generate changes in cell shape, size, or both, which can be comparable to the dimensions of the cell itself. However, the metaphor of cell as machine is in several regards misleading. Unlike machines, cells do not have specialized components connected to only a few other components and designed specifically to perform only one distinct function. Rather, connections are established by a limited number of components (such as genes and proteins) to perform multiple cellular functions. As such, the notion of cell as machine may lead to misunderstandings about how the eukaryotic cell actually works, down to the level of the gene, and even how the earliest eukaryotic cells came to be.

One key function of the eukaryotic cell is deformability, which is well characterized phenomenologically yet remains poorly understood fundamentally. When the cell is at rest, molecular fluctuations within its cytoskeletal network are not dominated by thermal fluctuations — as in colloidal materials at equilibrium and as assumed in traditional theories of viscoelasticity — but rather by the ongoing hydrolysis of adenosine triphosphate (ATP), which releases about 20 thermal units of energy per hydrolysis event. Einstein's fluctuation-dissipation theorem (which relates a system's fluctuations at thermal equilibrium and its response to external perturbations) and anything that depends on it thus fail dramatically^{1,2}. Moreover, for imposed strains of about 1% or smaller, the rheology of the cytoskeleton is strongly coupled to the active contractile stresses that it generates³, is highly sensitive to water content and the associated molecular crowding⁴, and is described universally by weak power laws. Therefore, cell rheology cannot be characterized by any defined scale of time⁵. Furthermore, for the larger deformations that characterize most of the physiological range, the cytoskeleton undergoes a remarkable transition from a solid-like to

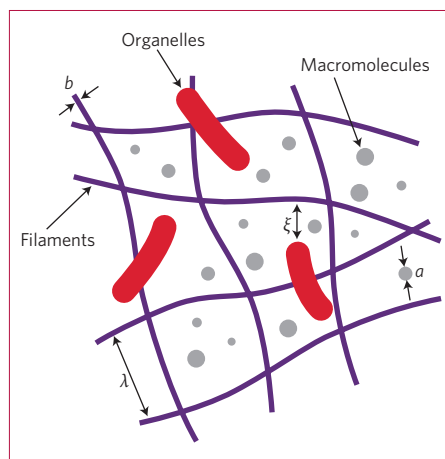


Figure 1 | The cytoskeleton behaves as a poroelastic material. It can be seen as a porous elastic solid meshwork (cytoskeleton, organelles, macromolecules) bathed in an interstitial fluid (cytosol)¹. Cellular rheology depends on the average filament diameter (b), the size of the particles in the cytosol (a), the hydraulic pore size (ξ) and the entanglement length of the cytoskeleton (λ).

a fluid-like state⁶. The cell's nucleus, which is stiffer than the cytoskeleton, also shares some of these same features⁷. Importantly, it is well recognized that these elastic cellular structures are porous and dispersed in water, which is of course the principal cellular constituent. Still, although the implications of water flow on cellular mechanics are known to be important⁴, the underlying mechanism has never been clear.

Writing in *Nature Materials*, Moendarbary and colleagues provide key clarifying insights. Using a combination of experiment and theory, they demonstrate that if an imposed cellular deformation is both big and fast enough to generate an appreciable change in local cytoplasmic volume, then the local restoring force that the cell generates can be understood as arising from poroelasticity⁸, that is, the redistribution of a viscous fluid flowing through a porous elastic matrix (Fig. 1) as occurs in the wringing of a water-filled sponge. Indeed, the authors show that, for a volume change of about $10 \mu\text{m}^3$, poroelasticity dominates for events faster

than roughly 0.5 s. If E is cytoskeletal elasticity, ξ is pore size and μ is cytosolic viscosity, then these fast events are characterized by a poroelastic diffusion constant D_p that scales as $D_p \sim E\xi^2/\mu$. Importantly, each of these three parameters carries a clear physical meaning and is experimentally accessible (Fig. 1). These insights should greatly enhance our understanding of acute dynamic events such as cell blebbing, and perhaps even protrusions of filopodia and lamellipodia. Of course, most mechanical events in biology are substantially slower or produce no appreciable change in cellular volume, yet for such events there is no comparable level of mechanistic understanding. Still, even in this circumscribed domain of big and fast events, how poroelastic timescales might relate to the almost-universal power-law behaviour reported in experiments spanning a similar time range⁹ (and also predicted by the glassy worm-like chain model) remains unclear. At different scales of length and time it is likely that the cell features a diverse range of relaxation mechanisms including molecular conformation changes, protein binding and unbinding, colloidal glassy dynamics, and, as highlighted by Moendarbary and co-authors, poroelastic cytosol flow.

Importantly, there is a broader context into which all these notions might be set. The cytoskeleton of the animal cell is closely comparable in its stiffness, rheology and malleability to a wide range of familiar inert mushy substances including pastes, foams, slurries and emulsions^{1,5,6}. In fact, although differing starkly in molecular detail, these materials share elastic moduli that are small and bounded to a narrow range (10^2 – 10^3 Pa). Are these similarities between inert and living soft matter a coincidence, or a clue? In the laboratory it is possible to use cytoskeletal building blocks to synthesize materials whose stiffness is orders of magnitude larger or smaller than that of the living cytoskeleton. If these building blocks can attain such a wide range of stiffnesses, why is the observed range so narrow in the living animal cell? Could it be that evolutionary pressure might have constrained the earliest eukaryotes to such a peculiar mush-like adaptation?

The last common ancestor of all eukaryotes, which lived roughly 2.4 billion years ago, was a motile single-celled heterotroph that ingested particulate organic matter¹⁰ by foraging in energy-rich microbial mats that were soft and paste-like¹¹. It has been argued that the cytoskeleton of this organism had adapted either to ingest microparticles (the phagotrophic hypothesis¹⁰) or to achieve motility¹¹. Clearly, had the cell's cytoskeleton been much softer than that of the mat, it would have been mechanically impossible for the cell to penetrate into it. On the other hand, a cytoskeleton that is substantially stiffer would have made motility within the mat metabolically wasteful. Efficient motility, therefore, should favour the adaptation of the cell's mechanical properties to match those of the energy-rich mush-like microbial mats within which it foraged¹¹. As a case in point, the environmental niche of the amoebozoan flagellate *Phalansterium*¹⁰, which may be the best surviving model of the eukaryotic last common ancestor, is the invasion of soft globular matrices (Fig. 2a).

More generally, an attractive evolutionary point of view reasons that living soft matter incorporates a limited number of ancient developmental motifs, each rooted in generic physical processes expressed by non-living soft matter¹². In these motifs, biological mechanisms seem to have bootstrapped soft-matter physics, which may have served as biology's starter kit¹². It has also been suggested that such mechanisms evolved so as to harness, leverage and elaborate these non-living physical effects, and then build on them a limited number of energy-dependent modules passed down to the present with few additions¹². Examples are the separation of immiscible inert fluids to yield differential cell adhesion and therefore resulting in cell sorting¹³, the

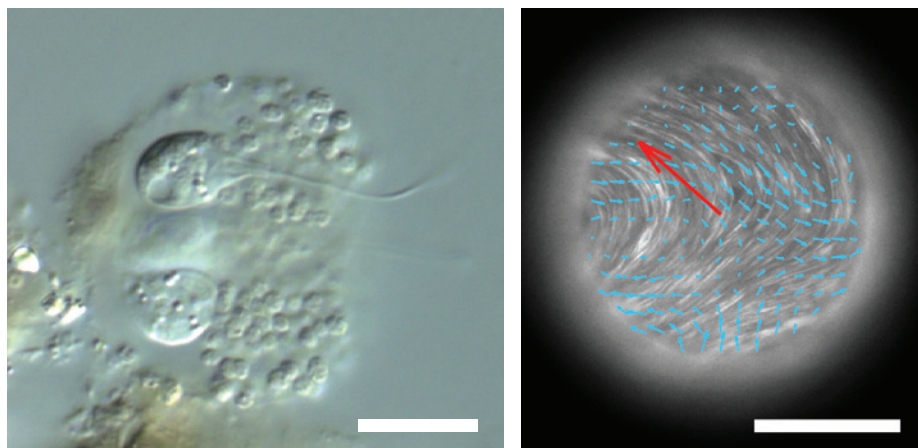


Figure 2 | The rheological properties of the cytoplasm of eukaryote cells compare to those of non-living soft matter. **a**, The amoebozoan flagellate *Phalansterium* invades soft globular matrices¹⁰. Scale bar, 10 μ m. **b**, In the presence of ATP, microtubule bundles self-organize and adsorb at an oil/water interface, creating streaming flows (denoted by blue arrows; the red arrow indicates the direction of instantaneous droplet velocity). Scale bar, 100 μ m. Figure reproduced with permission from: **a**, © David Patterson; **b**, ref. 15, © 2012 NPG.

glass transition between fluid- or solid-like states to yield collective cellular migration¹⁴, and simple suspensions comprising microtubules in water, which can harness ATP to self-organize and subsequently create active organized streaming flows (Fig. 2b). All this hints to the possibility that cytoskeletal origins are mush-like. If true, then the contemporary cell might be seen as a programmable, strongly linked signalling core that is adapted to harness non-programmable, weakly linked physical interactions. It is perhaps in this way that biological entities manage to attain stability together with evolvability. □

Enhua H. Zhou¹, Fernando D. Martinez² and Jeffrey J. Fredberg¹ are at the ¹Harvard School of Public Health, Boston, Massachusetts

02115, USA, ²University of Arizona, Tucson, Arizona 85724, USA.

e-mail: jfredber@hsph.harvard.edu

References

1. Bursac, P. *et al.* *Nature Mater.* **4**, 557–571 (2005).
2. Einstein, A. *Ann. Physik* **19**, 371–381 (1905).
3. Stamenovic, D. *Acta Biomaterialia* **1**, 255–262 (2005).
4. Zhou, E. H. *et al.* *Proc. Natl Acad. Sci. USA* **106**, 10632–10637 (2009).
5. Fabry, B. *et al.* *Phys. Rev. Lett.* **87**, 148102 (2001).
6. Treppe, X. *et al.* *Nature* **447**, 592–595 (2007).
7. Dahl, K. N., Engler, A. J., Pajerowski, J. D. & Discher, D. E. *Biophys. J.* **89**, 2855–2864 (2005).
8. Moenendary, E. *et al.* *Nature Mater.* **12**, 253–261 (2013).
9. Wolff, L., Fernandez, P. & Kroy, K. *PLoS ONE* **7**, e40063 (2012).
10. Cavalier-Smith, T. *Int. J. Syst. Evol. Microbiol.* **52**, 297–354 (2002).
11. Krishnan, R. *et al.* *PLoS ONE* **4**, e5486 (2009).
12. Newman, S. A. *Science* **338**, 217–219 (2012).
13. Steinberg, M. S. *Curr. Opin. Genet. Dev.* **17**, 281–286 (2007).
14. Angelini, T. E. *et al.* *Proc. Natl Acad. Sci. USA* **108**, 4714–4719 (2011).
15. Sanchez, T., Chen, D. T., DeCamp, S. J., Heymann, M. & Dogic, Z. *Nature* **491**, 431–434 (2012).

SPIDER SILK

Webs measure up

The complete elastic response of a spider's orb web has been quantified by non-invasive light scattering, revealing important insights into the architecture, natural material use and mechanical properties of the web. This knowledge advances our understanding of the prey-catching process and the role of supercontraction therein.

Zhao Qin and Markus J. Buehler

Developing advanced materials based on principles learnt from natural ones, like silk, can be an alternative to the laborious trial-and-error approach conventionally used. Even though silk's superb mechanical properties

have been known for decades, only recent work has shown that multiple length scales (from nanometre to metre) in its complex architecture contribute to the performance of orb webs, cob webs, sheet webs, funnel webs and other structures

like cocoons^{1–6}. Orb webs, in particular, are exceptional structures from a mechanical and an aesthetic point of view, and are constructed from hierarchically organized simple proteins (Fig. 1). To achieve certain properties, mechanisms interact

The cytoplasm of living cells behaves as a poroelastic material

Emad Moeendarbary^{1,2}, Léo Valon^{1,3}, Marco Fritzsche^{1,4}, Andrew R. Harris^{1,4}, Dale A. Moulding⁵, Adrian J. Thrasher⁵, Eleanor Stride⁶, L. Mahadevan^{7*} and Guillaume T. Charras^{1,8*}

The cytoplasm is the largest part of the cell by volume and hence its rheology sets the rate at which cellular shape changes can occur. Recent experimental evidence suggests that cytoplasmic rheology can be described by a poroelastic model, in which the cytoplasm is treated as a biphasic material consisting of a porous elastic solid meshwork (cytoskeleton, organelles, macromolecules) bathed in an interstitial fluid (cytosol). In this picture, the rate of cellular deformation is limited by the rate at which intracellular water can redistribute within the cytoplasm. However, direct supporting evidence for the model is lacking. Here we directly validate the poroelastic model to explain cellular rheology at short timescales using microindentation tests in conjunction with mechanical, chemical and genetic treatments. Our results show that water redistribution through the solid phase of the cytoplasm (cytoskeleton and macromolecular crowders) plays a fundamental role in setting cellular rheology at short timescales.

One of the most striking features of eukaryotic cells is their capacity to change shape in response to environmental or intrinsic cues driven primarily by their actomyosin cytoskeleton. During gross changes in cell shape, induced either by intrinsic switches in cell behaviour (for example, cell rounding, cytokinesis, cell spreading or cell movement) or by extrinsic stress application during normal organ function, the maximal rate at which shape change can occur is dictated by the rate at which the cytoplasm can be deformed because it forms the largest part of the cell by volume. Furthermore, it is widely recognized that cells detect, react and adapt to external mechanical stresses. However, in the absence of an in-depth understanding of cell rheology, the transduction of external stresses into intracellular mechanical changes is poorly understood, making the identification of the physical parameters that are detected biochemically purely speculative¹.

Living cells are complex materials exhibiting a high degree of structural hierarchy and heterogeneity coupled with active biochemical processes that constantly remodel their internal structure. Therefore, perhaps unsurprisingly, they exhibit an astonishing variety of rheological behaviours depending on amplitude, frequency and spatial location of loading^{1,2}. Over the years, a rich phenomenology of rheological behaviours has been uncovered in cells, such as scale-free power-law rheology, strain stiffening, anomalous diffusion, and rejuvenation (reviewed in refs 1–4). Several theoretical models explain these observed behaviours, but finding a unifying theory has been difficult because different microrheological measurement techniques excite different modes of relaxation¹. These rheological models range from those that treat the cytoplasm as a single-phase material whose rheology is described using networks of spring and dashpots⁵, to the sophisticated soft glassy rheology

models that describe cells as being akin to soft glassy materials close to a glass transition^{6,7}; in either case, the underlying geometrical and biophysical phenomena remain poorly defined^{1,4}. Furthermore, none of the models proposed account for dilatational changes in the multiphase material that is the cytoplasm. Yet, these volumetric deformations are ubiquitous in the context of phenomena such as blebbing, cell oscillations or cell movement^{8,9}, and in gels of purified cytoskeletal proteins¹⁰ whose macroscopic rheological properties depend on the gel structural parameters and its interaction with an interstitial fluid^{11–13}. Any unified theoretical framework that aims to capture the rheological behaviours of cells and link these to cellular structural and biological parameters must account for both the shear and dilatational effects seen in cell mechanics as well as include the role of crowding and active processes in cells.

The flow of water plays a critical part in such processes. Recent experiments suggest that pressure equilibrates slowly within cells (~10 s; refs 8,14,15) giving rise to intracellular flows of cytosol^{9,16} that cells may exploit to create lamellipodial protrusions⁹ or blebs⁸ for locomotion¹⁷. Furthermore, the resistance to water flow through the soft porous structure serves to slow motion in a simple and ubiquitous way that does not depend on the details of structural viscous dissipation in the cytoplasmic network. On the basis of these observations, a coarse-grained biphasic description of the cytoplasm as a porous elastic solid meshwork bathed in an interstitial fluid (for example, poroelasticity¹⁸ or the two-fluid model¹⁹) has been proposed as a minimal framework for capturing the essence of cytoplasmic rheology^{8,15,20}. In the framework of poroelasticity, coarse graining of the physical parameters dictating cellular rheology accounts for the effects of the interstitial fluid and related volume changes, macromolecular crowding and the cytoskeletal network^{8,15,21}, consistent with the rheological properties

¹London Centre for Nanotechnology, University College London, London WC1H 0AH, UK, ²Department of Mechanical Engineering, University College London, London WC1E 7JE, UK, ³Department of Physics, Ecole Normale Supérieure, Paris 75005, France, ⁴Department of Physics and Astronomy, University College London, London WC1E 6BT, UK, ⁵Molecular Immunology Unit, Institute of Child Health, University College London, London WC1N 1EH, UK, ⁶Institute of Biomedical Engineering, Department of Engineering Science, University of Oxford, Oxford OX1 3PJ, UK, ⁷School of Engineering and Applied Sciences, Department of Physics, Harvard University, Cambridge, Massachusetts 02138, USA, ⁸Department of Cell and Developmental Biology, University College London, London WC1E 6BT, UK. *e-mail: lm@seas.harvard.edu; g.charras@ucl.ac.uk.

of the cell on the timescales needed for redistribution of intracellular fluids in response to localized deformation. The response of cells to deformation then depends only on the poroelastic diffusion constant, D_p , with larger values corresponding to more rapid stress relaxations. This single parameter scales as $D_p \sim E\xi^2/\mu$, with E the drained elastic modulus of the solid matrix, ξ the radius of pores in the solid matrix, and μ the viscosity of the cytosol (see Supplementary Information), allowing changes in cellular rheology to be predicted in response to changes in E , ξ and μ .

Here, we probed the contribution of intracellular water redistribution to cellular rheology at timescales relevant to cell physiology (up to 10 s), and examined the relative importance of crowding and the cytoskeleton in determining cell rheology. To confirm the generality of our findings across cell types, our experiments examined HT1080 fibrosarcoma, HeLa cervical cancer cells, and Madin-Darby canine kidney (MDCK) epithelial cells.

Results

Cellular force–relaxation at short timescales is poroelastic.

First, we established the experimental conditions under which water redistribution within the cytoplasm might contribute to force–relaxation. In our experiments (Fig. 1a), following rapid indentation with an atomic force microscope (AFM) cantilever (3.5–6 nN applied during a rise time $t_r \sim 35$ ms resulting in $\delta \sim 1 \mu\text{m}$ cellular indentation), the force decreased by $\sim 35\%$ whereas indentation depth only increased by less than $\sim 5\%$, showing that our experiments measure force–relaxation under approximately constant applied strain (Fig. 1b,c). Relaxation in poroelastic materials is due to water movement out of the porous matrix in the compressed region. The timescale for water movement is $t_p \sim L^2/D_p$ (L is the length scale associated with indentation²²: $L \sim \sqrt{R\delta}$, with R the radius of the indenter) and therefore poroelastic relaxation contributes significantly if the rate of force application is faster than the rate of water efflux: $t_r \ll t_p$. Previous experiments estimated $D_p \sim 1\text{--}100 \mu\text{m}^2 \text{s}^{-1}$ in cells^{8,15}, yielding a characteristic poroelastic time of $t_p \sim 0.1\text{--}10$ s, far longer than t_r . Hence, if intracellular water redistribution is important for cell rheology, force–relaxation curves should exhibit characteristic poroelastic signatures for times up to $t_p \sim 0.1\text{--}10$ s.

Population averaged force–relaxation curves showed similar trends for both HeLa and MDCK cells, with a rapid decay in the first 0.5 s followed by slower decay afterwards (Fig. 1d(I)). In Fig. 1d(II), we see that force–relaxation clearly exhibited two separate regimes: a plateau lasting $\sim 0.1\text{--}0.2$ s followed by a transition to a linear regime (Fig. 1d(II)). Hence, at short timescales, cellular force–relaxation does not follow a simple power law. Comparison with force–relaxation curves acquired on physical hydrogels^{22,23}, which exhibit a plateau at short timescales followed by a transition to a second plateau at longer timescales (Supplementary Fig. S3A,B), suggests that the initial plateau observed in cellular force–relaxation may correspond to poroelastic behaviour. Indeed poroelastic models fitted the force–relaxation data well for short times (<0.5 s), whereas power-law models were applicable for times longer than $\sim 0.1\text{--}0.2$ s (Fig. 1d(II)). Finally, when force–relaxation curves acquired for different indentation depths on cells were renormalized for force and rescaled with a timescale dependent on indentation depth, all experimental curves collapsed onto a single master curve for short timescales, confirming that the initial dynamics of cellular force–relaxation are due to intracellular water flow (Supplementary Figs S1–S3, Results). Together, these data suggested that for timescales shorter than ~ 0.5 s, intracellular water redistribution contributed strongly to force–relaxation, consistent with the ~ 0.1 s timescale measured for intracellular water flows in the cytoplasm of HeLa cells²⁴.

To provide baseline behaviour for perturbation experiments, we measured the elastic and poroelastic properties of MDCK, HeLa

and HT1080 cells by fitting force-indentation and force–relaxation curves with Hertzian and poroelastic models, respectively. Measurement of average cell thickness suggested that, for timescales shorter than 0.5 s, cells could be considered semi-infinite and forces relaxed according to an exponential relationship: $F(t) \sim e^{-D_p t/L^2}$ (Supplementary Results, Fig. S10). In our experimental conditions (3.5–6 nN of force resulting in indentation depths less than 25% of cell height, Supplementary Fig. S4C,D), force–relaxation with an average amplitude of 40% was observed with 80% of total relaxation occurring in ~ 0.5 s (Fig. 1b,d). Analysis of the indentation curves yielded an elastic modulus of $E = 0.9 \pm 0.4$ kPa for HeLa cells ($N = 189$ curves on $n = 25$ cells), $E = 0.4 \pm 0.2$ kPa for HT1080 cells ($N = 161$ curves on $n = 27$ cells), and $E = 0.4 \pm 0.1$ kPa for MDCK cells ($n = 20$ cells). Poroelastic models fitted experimental force–relaxation curves well (on average $r^2 = 0.95$, black line, Fig. 1b(II)) and yielded a poroelastic diffusion constant of $D_p = 41 \pm 11 \mu\text{m}^2 \text{s}^{-1}$ for HeLa cells, $D_p = 40 \pm 10 \mu\text{m}^2 \text{s}^{-1}$ for HT1080 cells, and $D_p = 61 \pm 10 \mu\text{m}^2 \text{s}^{-1}$ for MDCK cells.

Poroelasticity predicts changes in rheology due to volume changes.

We examined the ability of the simple scaling law $D_p \sim E\xi^2/\mu$ to qualitatively predict changes in D_p resulting from changes in pore size due to a cell-volume change, which should not affect cytoskeletal organisation or integrity but should alter cytoplasmic pore size. We exposed HeLa and MDCK cells to hyperosmotic media to decrease the cell volume and hypoosmotic media to increase it, and measured concomitant changes in D_p .

First, we ascertained that osmotically induced volume changes persisted long enough for experimental measurements to be affected, and that control cells retained a constant volume over the same period of time (Fig. 2a). To ensure a stable volume increase in hypoosmotic conditions, we treated cells with regulatory volume decrease inhibitors²⁵ and measured a stable increase of $22 \pm 2\%$ in cell volume after hypoosmotic treatment (Fig. 2a). Conversely, on addition of 110 mM sucrose, cell volume decreased by $21 \pm 6\%$ (Fig. 2a), and on addition of PEG-400 (30% volumetric concentration), cell volume decreased drastically by $54 \pm 3\%$ (Fig. 2a and Supplementary Fig. S1E). Similar results were obtained for both cell types.

Next, we investigated whether changes in cell volume resulted in changes in poroelastic diffusion constant in both cell types. Consistent with results by others²⁶, our experiments revealed that cells relaxed less rapidly and became stiffer with decreasing fluid fraction. Increases in cell volume resulted in a significant increase in the poroelastic diffusion constant D_p and a significant decrease in cellular elasticity E (Fig. 2b,c). In contrast, a decrease in cell volume decreased the diffusion constant and increased elasticity (Fig. 2b,c). We verified that cytoskeletal organization was not perturbed by changes in cell volume (Supplementary Fig. S5 for actin), suggesting that the change in pore size alone was responsible for the observed changes in D_p and E . Because the exact relationship between hydraulic pore size ξ and cell volume is unknown, we plotted D_p and E as a function of the change in the volumetric pore size $\psi \sim (V/V_0)^{1/3}$. For both MDCK and HeLa cells, D_p scaled with ψ and the cellular elasticity E scaled inversely with ψ (Fig. 2d). In summary, an increase in cell volume increased the poroelastic diffusion constant and a decrease in cell volume decreased D_p , which is consistent with our simple scaling law.

Changes in cell volume perturb the cytoplasmic pore size. Having shown that changes in cell volume result in changes in the poroelastic diffusion constant without affecting cytoskeletal structure, we tried to directly detect changes in pore size. To do this, we microinjected PEG-passivated quantum dots (~ 14 nm hydrodynamic

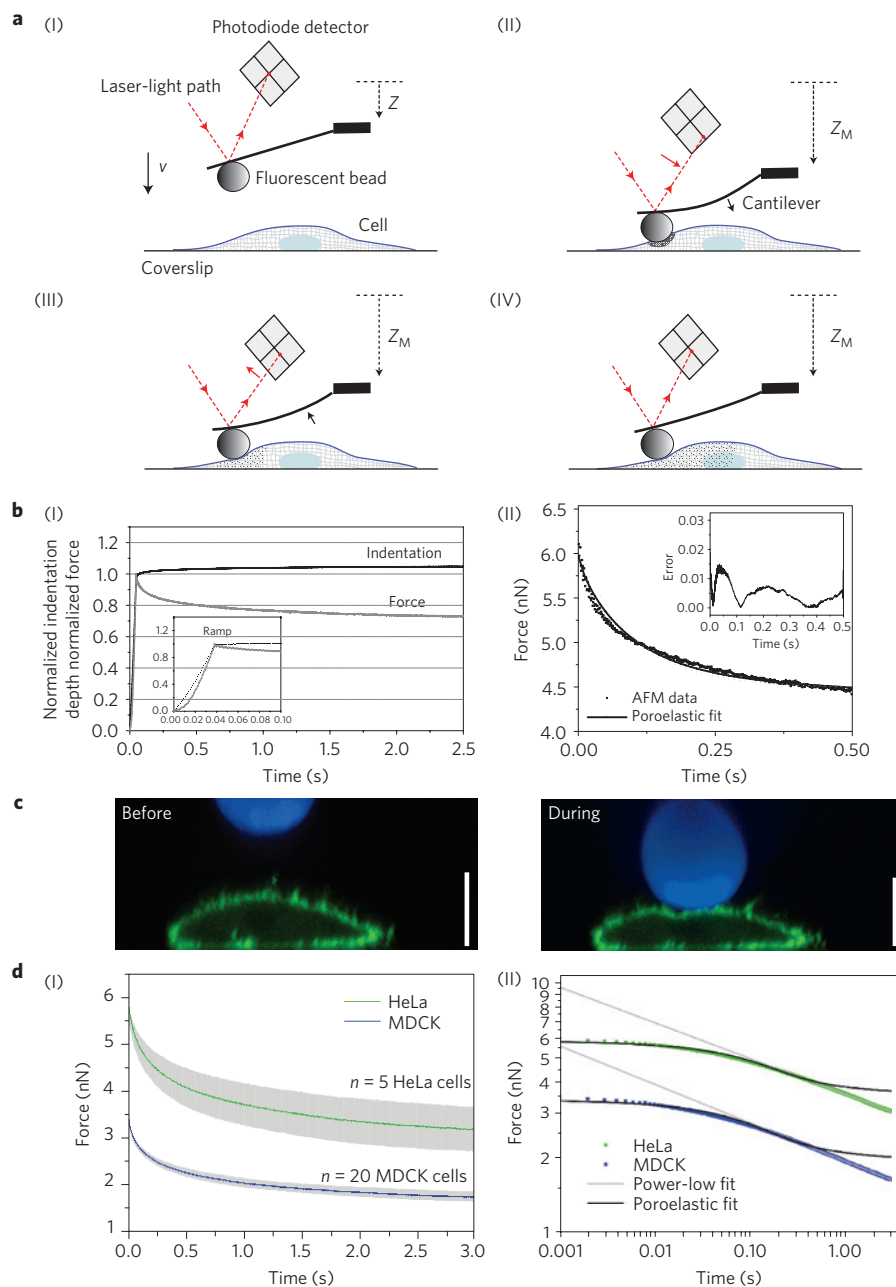


Figure 1 | Experimental set-up and functional form of cellular force-relaxation. **a**, Schematic diagram of the experiment. (I), The AFM cantilever is lowered towards the cell surface with a high approach velocity $V_{\text{approach}} \sim 10\text{--}30 \mu\text{m s}^{-1}$. (II), On contacting the cell surface, the cantilever bends and the bead starts indenting the cytoplasm. Once the target force F_M is reached, the movement of the piezoelectric ceramic is stopped at Z_M . The bending of the cantilever reaches its maximum. This rapid force application causes a sudden increase in the local stress and pressure inside the cell. (III), (IV), Over time, the cytosol in the compressed area redistributes inside the cell and the pore pressure dissipates. Strain resulting from the local application of force propagates through the elastic meshwork and, at equilibrium, the applied force is entirely balanced by cellular elasticity. Indentation (I–II) allows the estimation of elastic properties, and relaxation (III–IV) allows the estimation of the time-dependent mechanical properties. In all panels, the red line shows the light path of the laser reflected on the cantilever, red arrows show the change in direction of the laser beam, black arrows show the direction of bending of the cantilever, and the small dots represent the propagation of strain within the cell. **b** (I), Temporal evolution of the indentation depth (black) and measured force (grey) in response to AFM microindentation normalized to the values corresponding to the conditions at which the target force is reached. Inset: approach phase from which the elasticity is calculated (grey curve). The total approach lasts ~ 35 ms. (II), The first 0.5 s of experimental force-relaxation curves were fitted with the poroelastic model (black line). Inset: percentage error defined as $|F_{\text{AFM}} - F_{\text{fit}}|/F_{\text{AFM}}$. **c**, Z-x confocal image of a HeLa cell expressing PH-PLC δ 1-GFP (a membrane marker) corresponding to phases (I) and (IV) of the experiment described in **a**. The fluorescent bead attached to the cantilever is shown in blue and the cell membrane is shown in green. Scale bar, 10 μ m. **d** (I), Population-averaged force-relaxation curves for HeLa cells (green) and MDCK cells (blue) for target indentation depths of 1.45 μ m for HeLa cells and 1.75 μ m for MDCK cells. Curves are averages of $n = 5$ HeLa cells and $n = 20$ MDCK cells. The grey shaded area around the average relaxation curves represents the standard deviation of the data. (II), Population-averaged force-relaxation curves for HeLa cells (green) and MDCK cells (blue) from **d** (I) plotted in a log-log scale. For both cell types, the experimental force-relaxation was fitted with poroelastic (black solid line) and power-law relaxations (grey solid line).

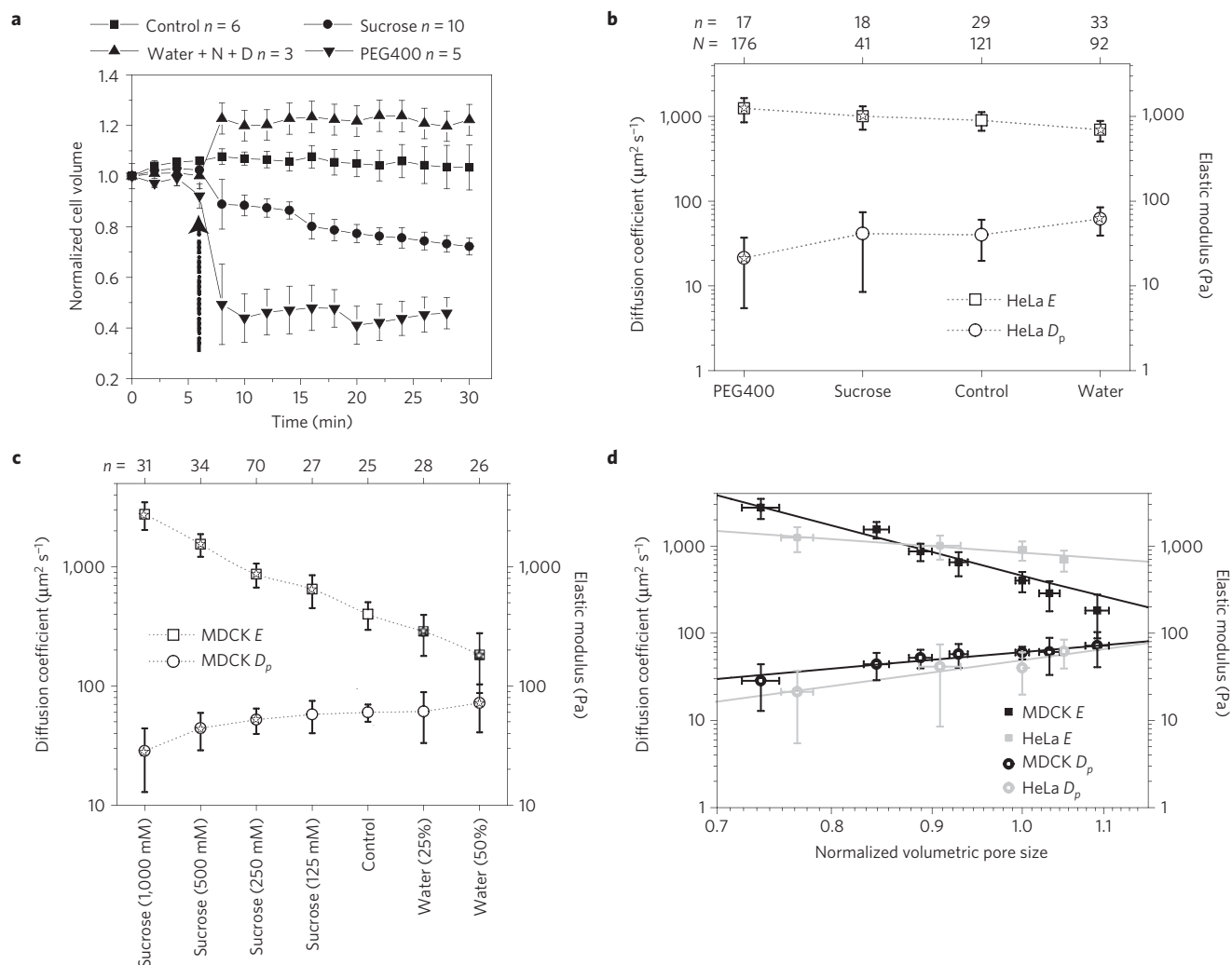


Figure 2 | Poroelastic and elastic properties change in response to changes in cell volume. **a**, Cell-volume change over time in response to changes in extracellular osmolarity. The volume was normalized to the initial cell volume at $t = 0$ s. The arrow indicates the time of addition of osmolytes. **b**, Effect of osmotic treatments on the elasticity E (squares) and poroelastic diffusion constant D_p (circles) in HeLa cells. **c**, Effect of osmotic treatments on the elasticity E (squares) and poroelastic diffusion constant D_p (circles) in MDCK cells. **d**, D_p and E plotted as a function of the normalized volumetric pore size $\psi \sim (V/V_0)^{1/3}$ in log-log plots for MDCK cells (black squares and circles) and HeLa cells (grey squares and circles). Straight lines were fitted to the experimental data points weighted by the number of measurements to reveal the scaling of D_p and E with changes in volumetric pore size (grey lines for HeLa cells, $E \sim \psi^{-1.6}$ and $D_p \sim \psi^{2.9}$, and black lines for MDCK cells, $E \sim \psi^{-5.9}$ and $D_p \sim \psi^{1.9}$). In all graphs, error bars indicate the standard deviation and, in graphs **b** and **c**, asterisks indicate significant changes ($P < 0.01$ compared with control). N indicates the total number of measurements and n indicates the number of cells. In hypoosmotic shock experiments, cells were incubated with 5-nitro-2-(3-phenylpropylamino) benzoic acid (NPPB) and 4-[(2-butyl-6,7-dichloro-2-cyclopentyl-2,3-dihydro-1-oxo-1H-inden-5-yl)oxy]butanoic acid (N + D on the graph), which are inhibitors of regulatory volume decrease.

radius with the passivation layer²⁷) into HeLa cells and examined their mobility. Under isoosmotic conditions, quantum dots rapidly diffused throughout the cell; however, on addition of PEG-400, they became immobile (Supplementary Movie and Fig. 3a, $n = 7$ cells examined). Hence, cytoplasmic pore size decreased in response to a cell-volume decrease trapping quantum dots in the cytoplasmic solid fraction and immobilizing them (Fig. 3d(II)). This suggested that the isoosmotic pore radius ξ was larger than 14 nm, consistent with our estimates from poroelasticity (Supplementary Results). Next, we verified that under hyperosmotic conditions cells retained a fluid fraction by monitoring recovery after photobleaching of a small fluorescein analogue (5-chloromethylfluorescein diacetate (CMFDA), hydrodynamic radius $R_h \sim 0.9$ nm; ref. 28). In isoosmotic conditions, CMFDA recovered rapidly after photobleaching (black line, Fig. 3b and Supplementary Table S1). In the presence of PEG-400, CMFDA fluorescence still recovered, indicating the

presence of a fluid phase, but recovery slowed by a factor of three, consistent with ref. 29 (grey line, Fig. 3b). The measured decrease in translational diffusion suggested a reduction in the cytoplasmic pore size with dehydration. Indeed, translational diffusion is related to the solid fraction Φ via the relation $D_T/D_{T\infty} \sim \exp(-\Phi)$, with $D_{T\infty}$ being the translational diffusion constant of the molecule in a dilute isotropic solution³⁰. Assuming that the fluid is contained in N pores of equal radius ξ , the solid fraction is $\Phi \sim V_s/(V_s + N\xi^3)$, with V_s being the volume of the solid fraction, a constant. $D_T/D_{T\infty}$ is therefore a monotonic increasing function of ξ . To study the effect of volume increase on pore size, we examined the fluorescence recovery after photobleaching of a cytoplasmic GFP decamer (enhanced green fluorescent protein EGFP-10 \times , $R_h \sim 7.5$ nm). Increases in cell volume resulted in a significant ~ 2 -fold increase in D_T ($P < 0.01$, Fig. 3c and Supplementary Table S1), suggesting that pore size did increase. Together, our experiments show that changes

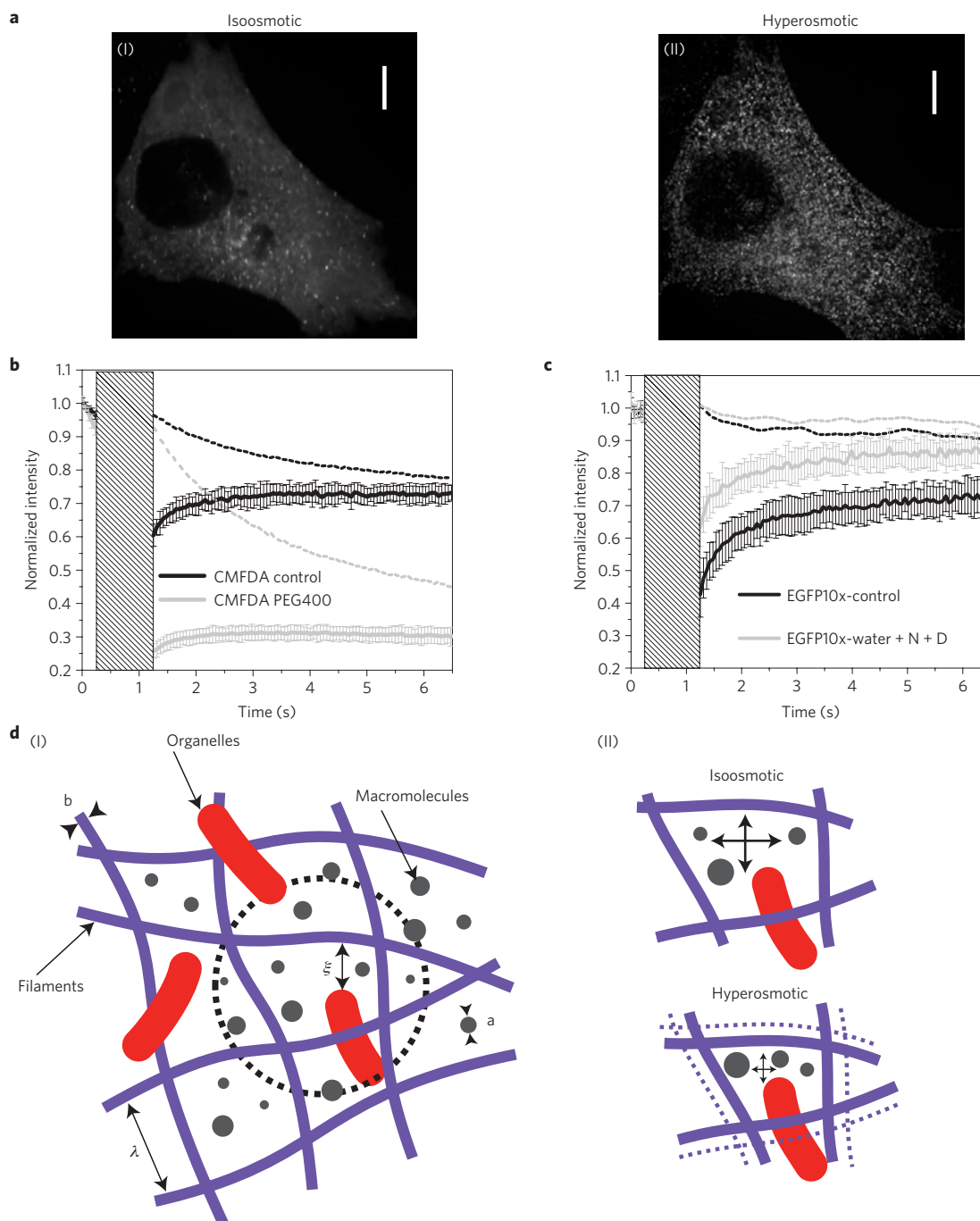


Figure 3 | Changes in cell volume change cytoplasmic pore size. **a**, Movement of PEG-passivated quantum dots microinjected into HeLa cells in isoosmotic conditions (I) and in hyperosmotic conditions (II). Both images are a projection of 120 frames totalling 18 s (Supplementary Movie). In isoosmotic conditions, quantum dots moved freely and the time-projection appeared blurry (I), whereas in hyperosmotic conditions quantum dots were immobile and the time-projected image allowed individual quantum dots to be identified (II). Images (I) and (II) are single confocal sections. Scale bars, 10 μm . **b**, Fluorescence recovery after photobleaching (FRAP) of CMFDA (a fluorescein analogue) in isoosmotic (black, $N = 19$ measurements on $n = 7$ cells) and hyperosmotic conditions (grey, $N = 20$ measurements on $n = 5$ cells). In both conditions, fluorescence recovered after photobleaching but the rate of recovery was decreased significantly in hyperosmotic conditions. **c**, FRAP of EGFP10x (a GFP decamer) in isoosmotic (black, $N = 17$ measurements on $n = 6$ cells) and hypoosmotic conditions (grey, $N = 23$ measurements on $n = 7$ cells). The rate of recovery was increased significantly in hypoosmotic conditions. In **b,c**, dashed lines indicate loss of fluorescence due to imaging in a region outside of the zone where FRAP was measured, and solid lines indicate fluorescence recovery after photobleaching. These curves are the average of N measurements, and error bars indicate the standard deviation for each time point. The greyed area indicates the duration of photobleaching. **d**, Schematic representation of the cytoplasm. (I) The cytoskeleton and macromolecular crowding participate in setting the hydraulic pore size through which water and solutes can diffuse. The length scales involved in setting cellular rheology are the average filament diameter b , the size a of particles in the cytosol, the hydraulic pore size ξ , and the entanglement length λ of the cytoskeleton. (II) Reduction in cell volume causes a decrease in entanglement length λ and an increase in crowding, which combined lead to a decrease in hydraulic pore size ξ .

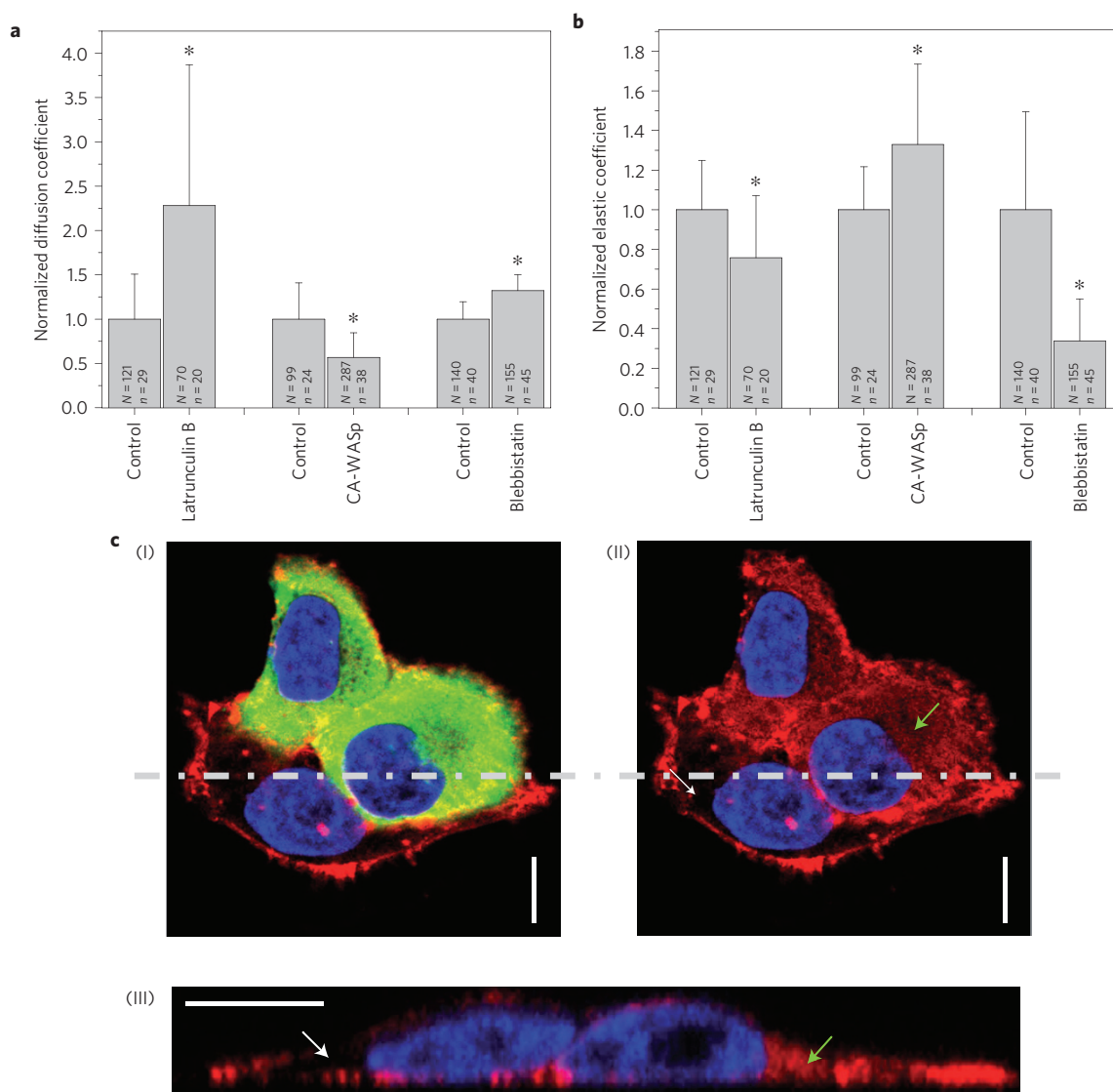


Figure 4 | The F-actin cytoskeleton is the main biological determinant of cellular poroelastic properties. **a**, Effect of F-actin depolymerization (Latrunculin treatment), F-actin overpolymerization (overexpression of CA-WASp), and myosin inhibition (blebbistatin treatment) on the poroelastic diffusion constant D_p . **b**, Effect of F-actin depolymerization, F-actin overpolymerization, and myosin inhibition on the cellular elasticity E . In **a, b**, asterisks indicate significant changes ($P < 0.01$). N is the total number of measurements and n the number of cells examined. **c**, Ectopic polymerization of F-actin due to CA-WASp. HeLa cells were transduced with a lentivirus encoding GFP-CA-WASp (in green) and stained for F-actin with rhodamine-phalloidin (in red). Cells expressing high levels of CA-WASp (green, I) had more cytoplasmic F-actin (red, II, green arrow) than cells expressing no CA-WASp (II, white arrow). (III) Z-x profile of the cells shown in (I) and (II) taken along the dashed line. Cells expressing CA-WASp exhibited more intense cytoplasmic F-actin staining (green arrow) than control cells (white arrow). Cortical actin fluorescence levels seemed unchanged. Nuclei are shown in blue. Images I and II are single confocal sections. Scale bars, 10 μm .

in cell volume modulate cytoplasmic pore size ξ consistent with estimates from AFM measurements (Supplementary Fig. S6A,B).

Poroelastic properties are influenced by the cytoskeleton. Cytoskeletal organization strongly influences cellular elasticity E (ref. 31), and is also likely to affect the cytoplasmic pore size ξ (Supplementary Fig. S7A–C). As both factors play antagonistic roles in setting D_p , we examined the effect of cytoskeletal perturbations.

Treatment of cells with 750 nM latrunculin, a drug that depolymerizes the actin cytoskeleton, resulted in a significant decrease in the cellular elastic modulus (Fig. 4b, consistent with ref. 31), a ~ 2 -fold increase in the poroelastic diffusion coefficient (Fig. 4a), and a significant increase in the lumped pore size (Supplementary Fig. S6E). Depolymerization of microtubules by treatment with 5 μM nocodazole had no significant effect

(Supplementary Fig. S6C–E). Stabilization of microtubules with 350 nM taxol resulted in a small (-16%) but significant decrease in elasticity but did not alter D_p (Supplementary Fig. S6C–E).

In light of the dramatic effect of F-actin depolymerization on D_p and ξ , we attempted to decrease the pore size by expressing a constitutively active mutant of WASp (WASp I294T, CA-WASp) that results in excessive polymerization of F-actin in the cytoplasm through ectopic activation of the arp2/3 complex, an F-actin nucleator (Fig. 4c; ref. 32). Increased cytoplasmic F-actin due to CA-WASp resulted in a significant decrease in the poroelastic diffusion coefficient (-43% , $P < 0.01$, Fig. 4a), a significant increase in cellular elasticity ($+33\%$, $P < 0.01$, Fig. 4b), and a significant decrease in the lumped pore size (-38% , $P < 0.01$, Supplementary Fig. S6E). Similar results were also obtained for HT1080 cells (-49% for D_p , $+68\%$ for E and -38% for

lumped pore size, $P < 0.01$). Then, we attempted to change cell rheology without affecting intracellular F-actin concentration by perturbing crosslinking or contractility. To perturb crosslinking, we overexpressed a deletion mutant of α -actinin (Δ ABD- α -actinin) that lacks an actin-binding domain but can still dimerize with endogenous protein³³, reasoning that this should either increase the F-actin gel entanglement length λ or reduce the average diameter of F-actin bundles b (Fig. 3d(I)). Overexpression of Δ ABD- α -actinin led to a significant decrease in E but no change in D_p or ξ (Fig. 4a,b and Supplementary Fig. S6E). Perturbation of contractility with the myosin II ATPase inhibitor blebbistatin (100 μ M) led to a 50% increase in D_p , a 70% decrease in E , and a significant increase in lumped pore size (Fig. 4a–b, Supplementary Fig. S6E).

To determine if ectopic polymerization of microtubules had similar effects to CA-WASp, we overexpressed γ -tubulin, a microtubule nucleator³⁴, but found that this had no effect on cellular elasticity, poroelastic diffusion constant, or lumped pore size (Supplementary Fig. S6C–E). Finally, expression of a dominant keratin mutant (Keratin 14 R125C; ref. 35) that causes aggregation of the cellular keratin intermediate filament network had no effect on E , D_p , or lumped pore size (Supplementary Figs S6C–E and S7C,D).

Discussion

Living cells exhibit poroelastic behaviours. We have shown that water redistribution plays a significant role in cellular responses to mechanical stresses at short timescales and that the effect of osmotic and cytoskeletal perturbations on cellular rheology can be understood in the framework of poroelasticity through a simple scaling law $D_p \sim E\xi^2/\mu$. Force–relaxation induced by fast localized indentation by AFM contained two regimes: at short timescales, relaxation was poroelastic; whereas at longer timescales, it exhibited a power law behaviour. We tested the dependence of D_p on the hydraulic pore size ξ by modulating cell volume, and showed that D_p scaled proportionally to volume change, which is consistent with a poroelastic scaling law. Changes in cell volume did not affect cytoskeletal organization but did modulate pore size. Experiments monitoring the mobility of microinjected quantum dots in HeLa cells suggested that ξ was ~ 14 nm, consistent with estimates based on measured values for D_p and E (Supplementary Results). We also confirmed that cellular elasticity scaled inversely to volume change, as shown experimentally^{26,36} and theoretically¹² for F-actin gels and cells. However, the exact relationship between the poroelastic diffusion constant D_p and the hydraulic pore size ξ could not be tested experimentally because the relationship between volumetric change and change in ξ is unknown due to the complex nature of the solid phase of the cytoplasm (composed of the cytoskeletal gel, organelles, and macromolecules, Fig. 3d(I); ref. 37). Taken together our results show that, for timescales up to ~ 0.5 s, the dynamics of cellular force–relaxation are consistent with a poroelastic behaviour for cells, and that changes in cellular volume resulted in changes in D_p due to changes in ξ .

Role of intracellular water redistribution in cell rheology. Cell mechanical studies over the years have revealed a rich phenomenological landscape of rheological behaviours that are dependent on probe geometry, loading protocol and loading frequency^{1–4}, although the biological origin of many of these regimes remains to be fully explored. Spurred on by recent reports implicating intracellular water flows in the creation of cellular protrusions^{8,9,16}, we have examined the role of intracellular water redistribution in cellular rheology. Our experimental measurements indicated that intracellular fluid flows occurred for deformations applied with a rise time t_r shorter than the poroelastic time $t_p \sim L^2/D_p$ (~ 0.2 s in our conditions), which is consistent with the timescales of intracellular water flows observed in HeLa S3 cells²⁴.

It may seem surprising that poroelastic effects have not been considered previously and we envisage several reasons for this. First, most studies to date have investigated cellular shear rheology using techniques such as magnetic twisting cytometry^{3,6,7} or bead tracking microrheology³⁸, which only account for isochoric deformations and thus cannot be used to study dilatational rheology where volumetric deformations, such as those induced in our experiments, arise. Second, the timescale of intracellular water flows is highly dependent on the volume of the induced deformation. Therefore, to observe poroelastic effects experimentally, large volumetric deformations must be induced and the cellular responses must be sampled at high rate (2,000 Hz in our experiments). Thus, although clues to poroelastic behaviours exist in previous experiments examining whole-cell deformation with optical stretchers (which reported a short timescale regime that could not be fit by power laws³⁹) and in previous AFM force–relaxation experiments (which reported the existence of a fast exponential decay occurring at short timescales^{40,41}), they were not systematically examined. Third, previous work¹¹ has shown that, in oscillatory experiments, for loading frequencies $f_p \gg E\xi^2/(\mu L^2)$ (~ 5 Hz in our experimental conditions), the fluid will not move relative to the mesh and therefore that inertial and structural viscous effects from the mesh are sufficient to describe the system. Hence, intracellular water flows participate in cell rheology for loadings applied with rise times t_r shorter than t_p and repeated with frequencies lower than f_p . Such a loading regime is particularly relevant for tissues of the cardiovascular and respiratory systems, where the constituent cells are routinely exposed to large strains applied at high strain rates and repeated at low frequencies (for example, 10% strain applied at $\sim 50\%$ s^{−1} repeated at up to 4 Hz for arterial walls⁴², 70% strain applied at up to 900% s^{−1} repeated at up to 4 Hz in the myocardial wall⁴³, and 20% strain applied at $> 20\%$ s^{−1} repeated at ~ 1 Hz for lung alveola⁴⁴). Further intuition for the significance of poroelastic effects during physiological cellular shape changes can be gained by computing a poroelastic Péclet number (see Supplementary Discussion).

Over the timescales of our experiments (~ 5 s), other factors such as turnover of cytoskeletal fibres and cytoskeletal network rearrangements due to crosslinker exchange or myosin contractility might also in principle influence cell rheology. In our cells, F-actin, the main cytoskeletal determinant of cellular rheology (Fig. 4 and refs 45,46), turned over with a half-time of ~ 11 s (Supplementary Fig. S7C), crosslinkers turned over in ~ 20 s (ref. 47), and myosin inhibition led to faster force–relaxation. Hence, active biological remodelling cannot account for the dissipative effects observed in our force–relaxation experiments. Taken together, the timescale of force–relaxation, the functional form of force–relaxation, and the qualitative agreement between the theoretical scaling of D_p with experimental changes to E and ξ support our hypothesis that water redistribution is the principal source of dissipation at short timescales in our experiments.

Hydraulic pore size is distinct from entanglement length. Although the cytoskeleton plays a fundamental role in modulating cellular elasticity and rheology, our studies show that microtubules and keratin intermediate filaments do not play a significant role in setting cellular rheological properties (Supplementary Fig. S6C–E). In contrast, both the poroelastic diffusion constant and elasticity strongly depended on actomyosin (Fig. 4). Our experiments qualitatively illustrated the relative importance of ξ and E in determining D_p . Depolymerizing the F-actin cytoskeleton decreased E and increased pore size, resulting in an overall increase in D_p . Conversely, when actin was ectopically polymerized in the cytoplasm by arp2/3 activation by CA-WASp (Fig. 4), E increased and the pore size decreased, resulting in a decrease in D_p . For both perturbations, changes in pore size ξ dominated over changes in cellular elasticity in setting D_p . For dense crosslinked F-actin gels, theoretical

relationships between the entanglement length λ and the elasticity E suggest that $E \sim \kappa^2/(k_B T \lambda^5)$ with κ the bending rigidity of the average F-actin bundle of diameter b , k_B the Boltzmann constant, and T the temperature¹² (Fig. 3d(I)). If the hydraulic pore size ξ and the cytoskeletal entanglement length λ were identical, D_p would scale as $D_p \sim \kappa^2/(\mu k_B T \lambda^3)$, implying that changes in elastic modulus would dominate over changes in pore size, in direct contradiction with our results. Hence, ξ and λ are different and ξ may be influenced both by the cytoskeleton and macromolecular crowding³⁷ (Fig. 3d(I)).

To decouple changes in elasticity from gross changes in intracellular F-actin concentration, we decreased E by reducing F-actin crosslinking through overexpression of a mutant α -actinin³³ that can either increase the entanglement length λ or decrease the bending rigidity κ of F-actin bundles by diminishing their average diameter b (Fig. 3d(I)). Overexpression of mutant α -actinin led to a decrease in E but no detectable change in D_p or ξ , confirming that pore size dominates over elasticity in determining cell rheology. Finally, myosin inhibition led to an increase in D_p , a decrease in E , and an increase in ξ , indicating that myosin contractility participates in setting rheology through application of pre-stress to the cellular F-actin mesh¹³, something that results directly or indirectly in a reduction in pore size^{13,48}. Taken together, these results show that F-actin plays a fundamental role in modulating cellular rheology, but further work will be necessary to understand the relationship between hydraulic pore size ξ , cytoskeletal entanglement length λ , crosslinking and contractility in living cells.

Cellular rheology and hydraulics. Although the poroelastic framework can mechanistically describe cell rheology at short timescales and predict changes of D_p in response to changes in microstructural and constitutive parameters, the minimal formulation provided here does not yet provide a complete framework for explaining the rich phenomenology of rheological behaviours observed over a wide range of timescales. However, building on the poroelastic framework's ability to link cell rheology to microstructural and constitutive parameters, it may be possible to extend its domain of applicability by including further molecular and structural detail, such as a more complex solid meshwork with the characteristics of a crosslinked F-actin gel¹² with continuous turnover and protein unfolding^{49,50}, or by considering the effects of molecular crowding on the movement of interstitial fluid.

Further intuition for the complexity and variety of length-scales involved in setting cellular rheology (Fig. 3d(I)) can be gained by recognizing that the effective viscosity μ felt by a particle diffusing in the cytosol will depend on its size (Fig. 3, Supplementary Fig. S5 and refs 51,52). Within the cellular fluid fraction, there exists a wide distribution of particle sizes, with a lower limit on the radius set by the radius of water molecules. Whereas measuring the poroelastic diffusion constant D_p remains challenging, the diffusivity D_m of any given particle can be measured accurately in cells. For a molecule of radius a , the Stokes–Einstein relationship gives $D_m = k_B T/(6\pi\mu a)$ or $\mu(a) = k_B T/(6\pi D_m a)$. Any interaction between the molecule and its environment (for example, reaction with other molecules, crowding and hydrodynamic interactions⁵³, and size-exclusion⁵²) will result in a deviation of the experimentally determined D_m from this relationship. Using the previous relationship for elasticity of gels and recalling that the bending rigidity of filaments scales as $\kappa \sim E_{\text{polymer}} b^4$ (with b the average diameter of a filament, or bundle of filaments, and E_{polymer} the elasticity of the polymeric material⁵⁴), we obtain the relationship

$$D_p \sim \left(\frac{\xi^2 a E_{\text{polymer}}^2 b^8}{(k_B T)^2 \lambda^5} \right) D_m$$

in which four different length scales contribute to setting cellular rheology. We see that the average filament bundle diameter b , the

size of the largest particles in the cytosol a (and indeed the particle size distribution in the cytosol), the entanglement length λ , and the hydraulic pore size ξ together conspire to determine the geometric, transport, and rheological complexity of the cell (Fig. 3d(I)). As all these parameters can be dynamically controlled by the cell, it is perhaps not surprising that a rich range of rheologies has been experimentally observed in cells^{1–7,9,10}.

Methods

Cell culture. Details on cell culture, drug treatments, and genetic treatments are provided in the Supplementary Information.

Atomic force microscopy measurements. During AFM experiments, measurements were acquired in several locations in the cytoplasm, avoiding the nucleus. To maximize the amplitude of stress relaxation, the cantilever tip was brought into contact with the cells using a fast approach speed ($V_{\text{approach}} \sim 10\text{--}30 \mu\text{m s}^{-1}$) until reaching a target force set to achieve an indentation depth $\delta \sim 1 \mu\text{m}$ (Fig. 1a(I),(II),b). Force was applied onto the cells in less than 35–100 ms, short compared with the experimentally observed relaxation time. On reaching the target force F_M the piezoelectric ceramic length was kept at a constant length and the force–relaxation curves were acquired at constant Z_M sampling at 2,000 Hz (Fig. 1a(III),(IV)). After 10 s, the AFM tip was retracted.

Measurement of the poroelastic diffusion coefficient. A brief description of the governing equations of linear isotropic poroelasticity and the relationship between the poroelastic diffusion constant D_p , the elastic modulus E , and hydraulic permeability k are given in Supplementary Information. We analysed our experiments as force–relaxation in response to a step displacement of the cell surface. No closed form analytical solution for indentation of a poroelastic infinite half-space by a spherical indenter exists. However, an approximate solution obtained by finite-element simulations gives²²:

$$\frac{F(t) - F_i}{F_i - F_i} = 0.491 e^{-0.908\sqrt{\tau}} + 0.509 e^{-1.679\tau} \quad (1)$$

where $\tau = D_p t / R \delta$ is the characteristic poroelastic time required for force to relax from F_i to F_f . Cells have a limited thickness h , and therefore the infinite half-plane approximation is only valid at timescales shorter than the time needed for fluid diffusion through the cell thickness: $t_{\text{hp}} \sim h^2 / D_p$. In our experiments on HeLa cells, we measured $h \sim 5 \mu\text{m}$ and $D_p \sim 40 \mu\text{m}^2 \text{s}^{-1}$, setting a timescale $t_{\text{hp}} \sim 0.6 \text{s}$. We confirmed numerically that for times shorter than $\sim 0.5 \text{s}$, approximating the cell to a half-plane gave errors of less than 20% (Supplementary Fig. S10). For short timescales, both terms in equation (1) are comparable and hence, as a first approximation, the relaxation scales as $\sim e^{-\tau}$. Equation (1) was used to fit our experimental relaxation data, with D_p as single fitting parameter, and we fitted only the first 0.5 s of relaxation curves to consider only the maximal amplitude of poroelastic relaxation and minimize errors arising from finite cell thickness.

Received 30 January 2012; accepted 5 December 2012;
published online 6 January 2013

References

- Hoffman, B. D. & Crocker, J. C. Cell mechanics: Dissecting the physical responses of cells to force. *Annu. Rev. Biomed. Eng.* **11**, 259–288 (2009).
- Fletcher, D. A. & Geissler, P. L. Active biological materials. *Annu. Rev. Phys. Chem.* **60**, 469–486 (2009).
- Trepat, X., Lenormand, G. & Fredberg, J. J. Universality in cell mechanics. *Soft Matter* **4**, 1750–1759 (2008).
- Kollmannsberger, P. & Fabry, B. Linear and nonlinear rheology of living cells. *Annu. Rev. Mater. Res.* **41**, 75–97 (2011).
- Bausch, A. R., Möller, W. & Sackmann, E. Measurement of local viscoelasticity and forces in living cells by magnetic tweezers. *Biophys. J.* **76**, 573–579 (1999).
- Fabry, B. *et al.* Scaling the microrheology of living cells. *Phys. Rev. Lett.* **87**, 148102 (2001).
- Deng, L. *et al.* Fast and slow dynamics of the cytoskeleton. *Nature Mater.* **5**, 636–640 (2006).
- Charras, G. T., Yarrow, J. C., Horton, M. A., Mahadevan, L. & Mitchison, T. J. Non-equilibration of hydrostatic pressure in blebbing cells. *Nature* **435**, 365–369 (2005).
- Keren, K., Yam, P. T., Kinkhabwala, A., Mogilner, A. & Theriot, J. A. Intracellular fluid flow in rapidly moving cells. *Nature Cell Biol.* **11**, 1219–1224 (2009).
- Bausch, A. R. & Kroy, K. A bottom-up approach to cell mechanics. *Nature Phys.* **2**, 231–238 (2006).
- Gittes, F., Schnurr, B., Olmsted, P. D., MacKintosh, F. C. & Schmidt, C. F. Microscopic viscoelasticity: shear moduli of soft materials determined from thermal fluctuations. *Phys. Rev. Lett.* **79**, 3286–3289 (1997).

12. Gardel, M. L. *et al.* Elastic behaviour of cross-linked and bundled actin networks. *Science* **304**, 1301–1305 (2004).
13. Mizuno, D., Tardin, C., Schmidt, C. F. & MacKintosh, F. C. Nonequilibrium mechanics of active cytoskeletal networks. *Science* **315**, 370–373 (2007).
14. Rosenbluth, M. J., Crow, A., Shaevitz, J. W. & Fletcher, D. A. Slow stress propagation in adherent cells. *Biophys. J.* **95**, 6052–6059 (2008).
15. Charras, G. T., Mitchison, T. J. & Mahadevan, L. Animal cell hydraulics. *J. Cell Sci.* **122**, 3233–3241 (2009).
16. Zicha, D. *et al.* Rapid actin transport during cell protrusion. *Science* **300**, 142–145 (2003).
17. Pollard, T. D. & Borisy, G. G. Cellular motility driven by assembly and disassembly of actin filaments. *Cell* **112**, 453–465 (2003).
18. Biot, M. A. General theory of three-dimensional consolidation. *J. Appl. Phys.* **12**, 155–164 (1941).
19. De Gennes, P. G. Dynamics of entangled polymer solutions (III). *Macromolecules* **9**, 587–598 (1976).
20. Mitchison, T. J., Charras, G. T. & Mahadevan, L. *Seminars in Cell Developmental Biology* vol. 19, 215–223 (Academic, 2008).
21. Dembo, M. & Harlow, F. Cell motion, contractile networks, and the physics of interpenetrating reactive flow. *Biophys. J.* **50**, 109–121 (1986).
22. Hu, Y., Zhao, X., Vlassak, J. J. & Suo, Z. Using indentation to characterize the poroelasticity of gels. *Appl. Phys. Lett.* **96**, 121904 (2010).
23. Kalcioğlu, Z. I., Mahmoodian, R., Hu, Y., Suo, Z. & Van Vliet, K. J. From macro- to microscale poroelastic characterization of polymeric hydrogels via indentation. *Soft Matter* **8**, 3393–3398 (2012).
24. Ibata, K., Takimoto, S., Morisaku, T., Miyawaki, A. & Yasui, M. Analysis of aquaporin-mediated diffusional water permeability by coherent anti-stokes raman scattering microscopy. *Biophys. J.* **101**, 2277–2283 (2011).
25. Hoffmann, E. K., Lambert, I. H. & Pedersen, S. F. Physiology of cell volume regulation in vertebrates. *Physiol. Rev.* **89**, 193–277 (2009).
26. Zhou, E. H. *et al.* Universal behaviour of the osmotically compressed cell and its analogy to the colloidal glass transition. *Proc. Natl Acad. Sci. USA* **106**, 10632–10637 (2009).
27. Derfus, A. M., Chan, W. C. W. & Bhatia, S. N. Intracellular delivery of quantum dots for live cell labelling and organelle tracking. *Adv. Mater.* **16**, 961–966 (2004).
28. Swaminathan, R., Bicknese, S., Periasamy, N. & Verkman, A. S. Cytoplasmic viscosity near the cell plasma membrane. *Biophys. J.* **71**, 1140–1151 (1996).
29. Kao, H. P., Abney, J. R. & Verkman, A. S. Determinants of the translational mobility of a small solute in cell cytoplasm. *J. Cell Biol.* **120**, 175–184 (1993).
30. Phillips, R. J. A hydrodynamic model for hindered diffusion of proteins and micelles in hydrogels. *Biophys. J.* **79**, 3350 (2000).
31. Rotsch, C. & Radmacher, M. Drug-induced changes of cytoskeletal structure and mechanics in fibroblasts: An atomic force microscopy study. *Biophys. J.* **78**, 520–535 (2000).
32. Moulding, D. A. *et al.* Unregulated actin polymerization by WASp causes defects of mitosis and cytokinesis in X-linked neutropenia. *J. Exp. Med.* **204**, 2213–2224 (2007).
33. Low, S. H., Mukhina, S., Srinivas, V., Ng, C. Z. & Murata-Hori, M. Domain analysis of α -actinin reveals new aspects of its association with F-actin during cytokinesis. *Exp. Cell Res.* **316**, 1925–1934 (2010).
34. Shu, H. B. & Joshi, H. C. Gamma-tubulin can both nucleate microtubule assembly and self-assemble into novel tubular structures in mammalian cells. *J. Cell Biol.* **130**, 1137–1147 (1995).
35. Werner, N. S. *et al.* Epidermolysis bullosa simplex-type mutations alter the dynamics of the keratin cytoskeleton and reveal a contribution of actin to the transport of keratin subunits. *Mol. Biol. Cell* **15**, 990–1002 (2004).
36. Spagnoli, C., Beyder, A., Besch, S. & Sachs, F. Atomic force microscopy analysis of cell volume regulation. *Phys. Rev. E* **78**, 31916 (2008).
37. Albrecht-Buehler, G. & Bushnell, A. Reversible compression of cytoplasm. *Exp. Cell Res.* **140**, 173–189 (1982).
38. Hoffman, B. D., Massiera, G., Van Citters, K. M. & Crocker, J. C. The consensus mechanics of cultured mammalian cells. *Proc. Natl Acad. Sci. USA* **103**, 10259–10264 (2006).
39. Wottawah, F. *et al.* Optical rheology of biological cells. *Phys. Rev. Lett.* **94**, 98103 (2005).
40. Darling, E. M., Zauscher, S. & Guilak, F. Viscoelastic properties of zonal articular chondrocytes measured by atomic force microscopy. *Osteoarthritis Cartilage* **14**, 571–579 (2006).
41. Moreno-Flores, S., Benitez, R., Vivanco, M. M. & Toca-Herrera, J. L. Stress relaxation and creep on living cells with the atomic force microscope: A means to calculate elastic moduli and viscosities of cell components. *Nanotechnology* **21**, 445101 (2010).
42. Avril, S., Schneider, F., Boissier, C. & Li, Z. Y. *In vivo* velocity vector imaging and time-resolved strain rate measurements in the wall of blood vessels using MRI. *J. Biomech.* **44**, 979–983 (2011).
43. Li, P. *et al.* Assessment of strain and strain rate in embryonic chick heart *in vivo* using tissue Doppler optical coherence tomography. *Phys. Med. Biol.* **56**, 7081–7092 (2011).
44. Perlman, C. E. & Bhattacharya, J. Alveolar expansion imaged by optical sectioning microscopy. *J. Appl. Physiol.* **103**, 1037–1044 (2007).
45. Van Citters, K. M., Hoffman, B. D., Massiera, G. & Crocker, J. C. The role of F-actin and myosin in epithelial cell rheology. *Biophys. J.* **91**, 3946–3956 (2006).
46. Treppe, X. *et al.* Universal physical responses to stretch in the living cell. *Nature* **447**, 592–595 (2007).
47. Mukhina, S., Wang, Y. & Murata-Hori, M. $[\alpha]$ -actinin is required for tightly regulated remodeling of the actin cortical network during cytokinesis. *Dev. Cell* **13**, 554–565 (2007).
48. Stewart, M. P. *et al.* Hydrostatic pressure and the actomyosin cortex drive mitotic cell rounding. *Nature* **469**, 226–230 (2011).
49. DiDonna, B. & Levine, A. J. Unfolding cross-linkers as rheology regulators in F-actin networks. *Phys. Rev. E* **75**, 041909 (2007).
50. Hoffman, B. D., Massiera, G. & Crocker, J. C. Fragility and mechanosensing in a thermalized cytoskeleton model with forced protein unfolding. *Phys. Rev. E* **76**, 051906 (2007).
51. Luby-Phelps, K., Castle, P. E., Taylor, D. L. & Lanni, F. Hindered diffusion of inert tracer particles in the cytoplasm of mouse 3T3 cells. *Proc. Natl Acad. Sci. USA* **84**, 4910–4913 (1987).
52. Dix, J. A. & Verkman, A. S. Crowding effects on diffusion in solutions and cells. *Annu. Rev. Biophys.* **37**, 247–263 (2008).
53. Ando, T. & Skolnick, J. Crowding and hydrodynamic interactions likely dominate *in vivo* macromolecular motion. *Proc. Natl Acad. Sci. USA* **107**, 18457–18462 (2010).
54. Gittes, F., Mickey, B., Nettleton, J. & Howard, J. Flexural rigidity of microtubules and actin filaments measured from thermal fluctuations in shape. *J. Cell Biol.* **120**, 923–934 (1993).

Acknowledgements

E.M. is in receipt of a Dorothy Hodgkin Postgraduate Award (DHPA) from the Engineering and Physical Sciences Research Council. L.M. thanks the MacArthur Foundation for support. G.T.C. is in receipt of a Royal Society University Research Fellowship. G.T.C., D.A.M. and A.J.T. are funded by Wellcome Trust grant (WT092825). M.F. was supported by a Human Frontier Science Program Young Investigator grant to G.T.C. The authors wish to acknowledge the UCL Comprehensive Biomedical Research Centre for generous funding of microscopy equipment. E.M. and G.T.C. thank R. Thorogate and C. Leung for technical help with the AFM set-up and Z. Wei for helpful discussions. We also gratefully acknowledge support of N. Ladommatos and W. Suen from Department of Mechanical Engineering at UCL.

Author contributions

E.M., L.M. and G.T.C. designed the research; E.M. and L.V. performed the research with some contributions from M.F. and D.M.; E.M. analysed the data; E.M., L.V., D.A.M., A.J.T. and G.T.C. generated reagents; E.M., L.V., M.F., A.R.H., E.S. and L.M. contributed analytical tools; E.M., L.M. and G.T.C. wrote the paper.

Additional information

Supplementary information is available in the online version of the paper. Reprints and permissions information is available online at www.nature.com/reprints. Correspondence and requests for materials should be addressed to L.M. or G.T.C.

Competing financial interests

The authors declare no competing financial interests.

The cytoplasm of living cells behaves as a poroelastic material

THEORY

Linear isotropic poroelasticity. The constitutive equations are adopted from¹ and are an extension of linear elasticity to poroelastic materials first introduced by Biot². Alternatively one can use the biphasic model³ that has been extensively applied in modelling the mechanics of cartilage and other soft hydrated tissues. The Biot formulation can be simplified when poroelastic parameters assume their limiting values. Under the “incompressible constituents” condition, the material exhibits its strongest poroelastic effect and the Biot poroelastic theory can be mathematically transformed to the biphasic model. We consider the quasi-static process of isotropic fully saturated poroelastic medium with constant porosity. The constitutive equation relates the total stress tensor $\boldsymbol{\sigma}$ to the infinitesimal strain tensor $\boldsymbol{\varepsilon}$ of the solid phase and the pore fluid pressure p :

$$\boldsymbol{\sigma} = 2G_s\boldsymbol{\varepsilon} + \frac{2G_s\nu_s}{(1-2\nu_s)}\{\text{tr } \boldsymbol{\varepsilon}\} \mathbf{I} - p\mathbf{I}, \quad (1)$$

where G_s and ν_s are the shear modulus and the Poisson ratio of the drained network respectively, \mathbf{I} the identity tensor, tr the trace operator and $\theta = \text{tr } \boldsymbol{\varepsilon}$ the variation in fluid content. This equation is similar to the constitutive governing equation for conventional single phase linear elastic materials. However the time dependent properties are incorporated through the pressure term acting as an additional external force on the solid phase. In the absence of body forces and neglecting the inertial terms the equilibrium equation $\text{div } \boldsymbol{\sigma} = 0$ results in:

$$G_s\nabla^2\mathbf{u} + \frac{G_s}{(1-2\nu_s)}\nabla \text{div } \mathbf{u} - \nabla p = 0, \quad (2)$$

where \mathbf{u} is the vector of solid displacement for small deformations $\boldsymbol{\varepsilon} = 0.5(\nabla\mathbf{u} + \nabla\mathbf{u}^T)$, div , ∇ and ∇^2 designate the divergence, gradient and Laplacian operators, respectively. Next, we consider fluid transport inside the porous medium through the introduction of Darcy’s law: $\mathbf{q} = -K\nabla p$, where \mathbf{q} is the filtration velocity and K the hydraulic permeability. Combining the continuity equation $\text{div } \mathbf{q} = -\partial\theta/\partial t$ and Darcy’s law yields:

$$\frac{\partial\theta}{\partial t} = K\nabla^2 p. \quad (3)$$

We obtain the diffusion equation for θ by combining equations (2) and (3) into what is called the consolidation equation:

$$\frac{\partial\theta}{\partial t} = D_p\nabla^2\theta, \quad (4)$$

where D_p is the poroelastic diffusion coefficient:

$$D_p = \frac{2G_s(1-\nu_s)}{(1-2\nu_s)}K \quad (5)$$

Derivation of the diffusion equation implies that under the assumptions made here, there are three independent parameters that characterize the mechanical properties of poroelastic cytoplasm: G_s , D_p , and ν_s .

Scaling of diffusion coefficient with microstructural parameters. The most important consequence of considering a poroelastic cytoplasm is that the macroscopic mechanical properties of the cell can be related to some coarse-grained cellular microstructural parameters. As a first step, to understand the relationship between microstructure and hydraulic permeability, we assume that pores within the solid matrix have an average radius of ξ . A simple analogy between a Poiseuille flow inside a tube with radius ξ and flow through the porous media with porosity φ leads to the following relationship for the hydraulic permeability K

$$K = \frac{\varphi}{4\kappa} \frac{\xi^2}{\mu}, \quad (6)$$

where μ is the viscosity of the fluid and κ is a constant taking into account the irregularity, interconnectivity and tortuosity of the pores⁴. Substituting this equivalent expression for the hydraulic permeability into equation (5) results in:

$$D_p = \left(\frac{(1 - \nu_s)}{(1 + \nu_s)(1 - 2\nu_s)} \frac{\varphi}{4\kappa} \right) \frac{E\xi^2}{\mu}. \quad (7)$$

As a first approximation, all of the parameters inside the parenthesis can be assumed to be a constant α and the functional dependence of all parameters with respect to the porosity of the structure is neglected. Therefore, a fundamental scaling law for poroelastic cytoplasm takes the form:

$$D_p = \alpha \frac{E\xi^2}{\mu}, \quad (8)$$

where μ is interpreted as the interstitial fluid viscosity, and $E = 2G_s / (1 + \nu_s)$ the elasticity of the constituent solid network.

METHODS

Cell culture. HeLa cells, HT1080, and MDCK cells were cultured at 37°C in an atmosphere of 5% CO₂ in air in DMEM (Gibco Life Technologies, Paisley, UK) supplemented with 10% FCS (Gibco Life Technologies) and 1% Penicillin/Streptomycin. Cells were cultured onto 50 mm glass bottomed Petri dishes (Fluorodish, World Precision Instruments, Milton Keynes, UK). Prior to the experiment, the medium was replaced with Leibovitz L-15 without phenol red (Gibco Life Technologies) supplemented with 10% FCS.

Generation of cell lines, transduction, and molecular biology. To enable imaging of the cell membrane, we created a stable cell line expressing the PH domain of Phospholipase C δ tagged with GFP (PHPLC δ -GFP), a phosphatidylinositol-4,5-bisphosphate binding protein that localises to the cell membrane. Briefly, PH-PLC δ -GFP (a kind gift from Dr Tamas Balla, NIH) was excised from EGFP-N1 (Takara-Clontech Europe, St Germain en Laye, France), inserted into the retroviral vector pLNCX2 (Takara-Clontech), and transfected into 293-GPG cells for packaging (a kind gift from Prof Daniel Ory, Washington University⁵). Retroviral supernatants were then used to infect wild type HeLa cells, cells were selected in the presence of 1 mg.ml⁻¹ G418 (Merck Biosciences UK, Nottingham, UK) for 2 weeks and subcloned to obtain a monoclonal cell line. Using similar methods, we created cell lines stably expressing cytoplasmic GFP for cell volume estimation, GFP-actin or Life-act Ruby⁶ (a kind gift of Dr Roland Wedlich-Soldner, MPI-Martinsried, Germany) for examination of the F-actin cytoskeleton, GFP-tubulin for examination of the microtubule cytoskeleton, and GFP-Keratin 18 (a kind gift of Dr Rudolf Leube, University of Aachen, Germany) for visualisation of the intermediate filament network. HT1080 cells expressing mCherry-LifeAct and MDCK cells expressing PHPLC δ -GFP were generated using similar methods. The EGFP-10x plasmid was described in⁷ and obtained through Euroscarf (Frankfurt, Germany). Cells were transfected with cDNA using lipofectamine 2000 according to manufacturer instructions the night before measurements.

Pharmacological treatments for disrupting the cytoskeleton. Cells were incubated in culture medium with the relevant concentration of drug for 30 min prior to measurement. The medium was then replaced with L-15 with 10% FCS plus the same drug concentration such that the inhibitor was present at all times during measurements. Cells were treated with latrunculin B (to depolymerise F-actin, Merck-Biosciences), nocodazole (to depolymerise microtubules, Merck-Biosciences), paclitaxel (to stabilize microtubules, Merck-Biosciences), and blebbistatin (to inhibit myosin II ATPase, Merck-Biosciences).

Genetic treatments for perturbing the cytoskeleton. To examine the effect of uncontrolled polymerization of cytoplasmic F-actin, we transduced HeLa cells stably expressing Life-act ruby with lentivirus encoding WASp I294T as described in⁸. Lentiviral vectors expressing enhanced GFP fused to human WASp with the I294T mutation were prepared in the pHR'SIN-cPPT-CE and pHR'SIN-cPPT-SE lentiviral backbones as described previously^{8,9}. Lentivirus was added to cells at a multiplicity of infection of 10 to achieve approximately 90% transduction.

To examine the effect of uncontrolled polymerisation of tubulin, we transfected HeLa cells with a plasmid encoding γ -tubulin, a microtubule nucleator¹⁰. γ -tubulin-SNAP¹¹ was obtained from Euroscarf, the SNAP tag was excised and replaced by mCherry. To disrupt the keratin network of HeLa cells, we overexpressed keratin 14 R125C-YFP (a kind gift from Prof Thomas Magin, University of Leipzig), a construct that acts as a dominant mutant and results in aggregation of endogenous keratins¹². To disrupt F-actin crosslinking by endogenous α -actinin, we transfected cells with a deletion mutant of α -actinin lacking an actin-binding domain (Δ ABD- α -actinin, a kind gift of Dr Murata-Hori, Temasek Life Sciences laboratory, Singapore). Cells were transfected with cDNA using lipofectamine 2000 the night before experimentation.

Visualising cytoplasmic F-actin. To visualise cytoplasmic F-actin density, cells were fixed for 15 minutes with 4% PFA at room temperature, permeabilised with 0.1% Triton-X on ice for 5 min, and passivated by incubation with phosphate buffered saline (PBS) and 10 mg/ml bovine serum albumin (BSA) for 10 min. They were then stained with Rhodamine-Phalloidin (Invitrogen) for 30 min at room temperature, washed several times with PBS-BSA, and mounted for microscopy examination on a confocal microscope.

Imaging of cell volume changes. To measure changes in cell volume in response to osmotic shock, confocal stacks of cells expressing cytoplasmic GFP were acquired at 2 min intervals using a spinning disk confocal microscope (Yokogawa CSU-22, Yokogawa, Japan) with 100x oil immersion objective lens (NA=1.3, Olympus, Berlin, Germany) and a piezo-electric z-drive (NanoscanZ, Prior, Scientific, Rockland, MA). Stacks consisted of

40 images separated by 0.2 μm and were acquired for a total of 30 min and captured on an Andor iXon EMCCD camera.

Changes in osmolarity

Changes in extracellular osmolarity were effected by adding a small volume of concentrated sucrose, 400-Dalton polyethylene glycol (PEG-400, Sigma-Aldrich,¹³), or water to the imaging medium. When increasing osmolarity by addition of osmolyte, we treated MDCK cells with EIPA (50 μM , Sigma-Aldrich), an inhibitor of regulatory volume increases¹⁴. When decreasing the osmolarity by addition of water, we treated the cells simultaneously with inhibitors of regulatory volume decreases, NPPB (200 μM ; Tocris, Bristol, UK) and DCPIB (50 μM , Tocris), to achieve a sustained volume increase. Cells were incubated with these inhibitors for 30 minutes prior to the addition of water.

Fluorescence and confocal imaging. In some experiments, we acquired fluorescence images of the cells using an IX-71 microscope interfaced to the AFM head and equipped with an EMCCD camera (Orca-ER, Hamamatsu, Germany) piloted using $\mu\text{Manager}$ (Micromanager, Palo-Alto, CA). Fluorophores were excited with epifluorescence and the appropriate filter sets and images were acquired with a 40x dry objective ($\text{NA}=0.7$). For staining of the nucleus, cells were incubated with Hoechst 34332 (1 $\mu\text{g}/\text{ml}$ for 5 min, Merck-Biosciences).

In some cases, to image the cellular indentation in zx -plane, we utilized an AFM interfaced to a confocal laser scanning microscope (FV1000, Olympus). Images were acquired with a 100x oil immersion objective lens ($\text{NA}=1.3$, Olympus). Latex beads attached to AFM cantilevers were imaged by exciting with a 647 nm laser and collecting light at 680 nm. GFP tagged proteins were excited with a 488 nm laser and light was collected at 525 nm. Ruby or Cherry tagged proteins were excited with a 568 nm laser and light was collected at 620 nm. zx -confocal images passing through the centre of the bead were acquired with 0.2 μm steps in z to give a side view of the cell before and during indentation or before and after change in extracellular osmolarity (Fig. 1C, Fig. S1F).

Calculating cell volume. Exposure time and laser intensity were optimised to minimize photobleaching. A custom written code in Matlab (Mathworks Inc, Cambridge, UK) was used to process the z stacks and measure the cell volume at each time point. Briefly, the background noise of stack images was removed, images were smoothed, and binarised using Matlab Image Processing Toolbox functions. Following binarization, series of erosion and dilatation operations were performed to create a contiguous cell volume image devoid of isolated pixels. The sum of non-zero pixels in each stack was multiplied by the volume of a voxel to give a measure of cell volume at each time step. All experiments followed the same protocol: five stacks were captured prior to changing osmolarity and then cell volume was followed for a further 25 minutes.

Atomic force Microscopy measurements. Force-distance and force-relaxation measurements were acquired with a JPK Nanowizard-I (JPK instruments, Berlin, Germany) interfaced to an inverted optical fluorescence microscope (IX-81 or IX-71, Olympus).

AFM cantilevers (MLCT, Bruker, Karlsruhe, Germany) were modified by gluing beads to the cantilever underside with UV curing glue (UV curing, Loctite, UK). Cantilever spring constants were determined prior to gluing the beads using the thermal noise method implemented in the AFM software (JPK SPM, JPK instruments). Prior to any cellular indentation tests, the sensitivity of the cantilever was set by measuring the slope of force-distance curves acquired on glass regions of the petri dish. For measurements on cells, we used cantilevers with nominal spring constants of 0.01 $\text{N}\cdot\text{m}^{-1}$ and fluorescent latex beads (ex645/em680, $R=7.5$ μm , Invitrogen). For measurements on hydrogels, we used cantilevers with nominal spring constants of 0.6 $\text{N}\cdot\text{m}^{-1}$ and glass beads ($R=25$ μm , Sigma).

During force-relaxation measurements, we used the z -closed loop feedback implemented on the JPK Nanowizard to maintain a constant z -piezo height. When acquiring force-relaxation curves with high approach velocities ($V_{\text{approach}} > 10$ $\mu\text{m}\cdot\text{s}^{-1}$), the first 5 ms of force-relaxation were not considered in the data analysis due to the presence of small oscillations in z -piezoelectric ceramic height immediately after contact. When acquiring force-relaxations curves for averaging over multiple cells, we used approach velocities $V_{\text{approach}} \sim 10$ $\mu\text{m}\cdot\text{s}^{-1}$ that did not give rise to oscillations in the length of the z -piezoelectric ceramic.

Hydrogels. For comparison with cells, we acquired force-relaxations measurements on physical hydrogels, which are well-characterised poroelastic materials. For measurements, we made gels with a 15% solution of a 20:1 mix of acrylamide-bis-acrylamide crosslinked with TEMED and ammonium persulfate following the manufacturer's instructions (Bio-Rad, UK).

Cell height and spatial measurements with AFM. To investigate spatial variations in the cellular poroelastic properties, we acquired measurements at several locations on the cell surface along the long axis of the cell with a target force of $F_M = 4$ nN. To locate indentation points on optical images of the cell, a fluorescence image of the bead resting on the glass surface close to the cell was acquired and the bead centre used as a reference point (see Fig. S9A). This reference point was used to estimate the height of the cell in each measurement point, as well as the position of indentation on the cell surface knowing the xy-coordinates of each stress relaxation measurement from the AFM software. The position of the measurement point relative to the nucleus was estimated by acquiring a fluorescence image of the nucleus and calculating its centre of mass (see Fig. S9A).

To measure cell height, we collected a force-distance curve on the glass substrate next to the cell being examined and the height of contact between the probe and the glass was used as a height reference (see Fig. S9A). At each indentation point, the cell height was estimated by comparing the height of contact to the reference. The position of contact in force-distance curves was determined using the algorithm described in ^{15,16}.

Measurement of indentation depth, cellular elastic modulus. The approach phase of AFM force-distance curves (inset, Fig. 1B-I) was analysed to extract the elastic modulus E which is linearly related to the shear modulus G through the Poisson ratio $E = 2G(1 + \nu)$. For estimation of the elastic modulus, we assumed a Poisson ratio $\nu = 0.3$. The contact point between the cell and the AFM tip was found using the method described in ^{15,16}. The indentation depth δ was calculated by subtracting the cantilever deflection d from the piezo translation z after contact $\delta = z - d$. E was estimated by fitting the contact portion of the curve with a Hertzian contact model between a sphere and an infinite half space ¹⁷. The relationship between the applied force F and the indentation depth is:

$$F = \frac{8}{3} \frac{G}{1 - \nu} R^{1/2} \delta^{3/2}, \quad (9)$$

with ν the Poisson ratio, and R the radius of the spherical indenter. To minimise errors arising from finite cell thickness, we excluded data points where the indentation depth δ was more than a quarter of the cell height h ¹⁸⁻²⁰.

In our experiments, the cantilever was approached at very high velocity and hence at short times the cytoplasmic interstitial fluid does not have time to drain out of the compressed region. This represents the undrained condition for the poroelastic material ^{1,21} and equation (9) becomes $F(0) = \frac{16}{3} GR^{1/2} \delta^{3/2}$. At long time-scales, the interstitial fluid redistributes in the cell and the force imposed by the indenter is balanced by stress in the elastic porous matrix only. Under this condition, the force applied for the prescribed indentation is $F(\infty) = \frac{8}{3(1 - \nu_s)} GR^{1/2} \delta^{3/2}$. Comparing the long time-scale and short time-scale limits allows for estimation of the Poisson ratio of the solid matrix $F(0)/F(\infty) = 2(1 - \nu_s)$. Experimental force-distance curves were analysed using custom written software in Matlab following the algorithm described in ¹⁵.

Establishing the experimental conditions to measure cellular poroelastic diffusion constant. In our experiments, after rapid local force application by AFM (6nN applied during a rise time t_r of 35ms on HeLa cells, Fig. 1A-B), the indentation depth increased by an average of $\sim 5\%$ over a 2.5s relaxation period ($N=189$ measurements, Fig. 1B-I, black), whereas force relaxed by $\sim 35\%$ (Fig. 1B-I, grey). Therefore, we assumed that the indentation depth and contact area remained constant and our experimental conditions are those of a force-relaxation problem. In poroelasticity, relaxation following application of force is due to water movement out of the porous matrix in the displaced region. Hence to truly probe the poroelastic properties of cells, we need to establish a regime where deformation is applied faster than water can leave the displaced volume. In an axisymmetric problem, this can be expressed simply by comparing the rise time t_r needed to reach an indentation depth δ to the time needed for water to diffuse out of the displaced volume $t_p \sim L^2/D_p$ with L the length-scale of the problem ^{22,23}: $L \sim (R\delta)^{0.5}$ with R the radius of the indenter. In our experiments, we used an indenter with radius $R = 7.5$ μm , a typical indentation depth $\delta = 1$ μm , and previous experiments suggested $D_p \sim 1$ to 100 $\mu\text{m}^2 \cdot \text{s}^{-1}$ ^{24,25} in cells yielding characteristic poroelastic times of $t_p \sim 0.1$ to 10 s. Hence, given an experimental rise time of $t_r \sim 35$ ms, t_r/t_p is small compared to 1 signifying that pressurisation of interstitial water occurs and therefore water movement through the solid matrix contributes strongly to relaxation.

Determining the apparent cellular viscosity. For comparison with previous reports and use in numerical models of cell dynamics, we determined the apparent cellular viscosity of cells in our experiments using a standard linear

model consisting of a spring-damper (stiffness k_1 and apparent viscosity η) in parallel with another spring (stiffness k_2), as described in ²⁶. In this model, the applied force decays exponentially when the material is subjected to a step displacement at $t=0$:

$$\frac{F(t) - F_f}{F_i - F_f} = e^{-\frac{k_1 t}{\eta}}. \quad (10)$$

The spring constant k_1 scales with the elastic modulus $k_1 \sim E$ and therefore we fitted our experimental force-relaxation curves using equation (10), with η as sole fitting parameter.

Microinjection and imaging of quantum dots. PEG-passivated quantum dots (qdots 705, Invitrogen) were diluted in injection buffer (50 mM potassium glutamate, 0.5 mM MgCl_2 , pH 7.0) to achieve a final concentration of 0.2 μM and microinjected into HeLa cells as described in ²⁷. Quantum dots were imaged on a spinning disk confocal microscope by exciting at 488nm and collecting emission above 680 nm. To qualitatively visualize the extent of quantum dot movement, time series were projected onto one plane using ImageJ.

FRAP experiments. FRAP experiments were performed using a 100x oil immersion objective lens (NA=1.3, Olympus) on a scanning laser confocal microscope (Olympus Fluoview FV1000; Olympus). Cytoplasmic fluorophores including GFP-tagged proteins and CMFDA (5-chloromethylfluorescein diacetate, Celltracker Green, Invitrogen) were excited at 488 nm wavelength. For experiments with CMFDA, cells were incubated with 2 μM CMFDA for 45 min before replacing the medium with imaging medium. For experiments with GFP or EGFP-10x, cells were transfected with the plasmid of interest the day before experimentation. To obtain a strong fluorescence signal and minimize photobleaching, a circular region of interest (ROI, 1.4 μm in diameter) in the middle of the cytoplasm was imaged setting laser power (488nm wave length, nominal output of 20mW) to 5% and 1% of maximum output for GFP and CMFDA, respectively. Each FRAP experiment started with five image scans, followed by a 1s bleach pulse produced by scanning the 488nm laser beam line by line (at 100% power for GFP and 25% power for CMFDA) over a circular bleach region of nominal radius $r_n=0.5 \mu\text{m}$ centered in the middle of the imaging ROI. To sample the recovery with sufficient time resolution, an imaging ROI of radius of 0.7 μm was chosen allowing acquisition with a rate of 50ms per frame.

Effective bleach radius. Because of rapid diffusion of fluorophores within the cytoplasm during the bleaching process, the effective radius over which photobleaching takes place (r_e) is larger than the nominal radius (r_n). We followed the methods described in ²⁸ to fit our FRAP experiments and hence needed to determine r_e . To experimentally estimate the effective radius r_e , we performed a separate series of FRAP experiments on cells loaded with CMFDA in hyperosmotic conditions. We empirically chose an imaging area larger than the effective photobleaching radius (4 μm in diameter) and imaged photobleaching recovery at a frame rate of 0.2s/frame. Next, using a custom written Matlab program, we calculated the radial projection profile of the fluorescence intensity in the imaging region for the first post-bleach image $I(r, t=1)$ and then fitted the experimental intensity profile with the bleach equation for a Gaussian laser beam to determine r_e ²⁸ (Fig. S8A):

$$I(r) = \exp\left(-K \exp\left(-2 \frac{r^2}{r_e^2}\right)\right), \quad (11)$$

where r is the radial distance from the centre of bleach spot and K is the bleaching constant related to the intensity of the bleaching laser and the properties of the fluorophore.

FRAP analysis. FRAP recovery curves $I(t)$ were obtained by normalising the mean fluorescence intensity within the nominal bleach area for each frame to the average fluorescence intensity of the first pre-bleach image. The translational diffusion coefficient D_T was estimated using the model for a uniform-disk laser profile and ideal bleach ^{29,30} following the methods described in ²⁸:

$$I_n(t) = \exp\left(-\frac{r_e^2}{8D_T t}\right) \left[I_0\left(\frac{r_e^2}{8D_T t}\right) + I_1\left(\frac{r_e^2}{8D_T t}\right) \right], \quad (12)$$

where $I_n(t) = I(t)/I(\infty)$ is the normalized fluorescence intensity in the bleached spot as a function of time t , r_e is the effective bleach radius, I_0 and I_1 are modified Bessel functions. In the experimentally acquired FRAP curves, the first post-bleach value $I_n(t=1s)$ was larger than zero (Fig. 3B,C), something that could be due to rapid fluorophore diffusion during the bleach process or incomplete bleaching²⁸. In cells exposed to hyperosmotic conditions, the intensity of the first post-bleach time point was over 30% lower than in isoosmotic conditions, suggesting that the non-zero value of this first time point was due to rapid diffusive recovery. Based on this observation, we assigned a timing of $t=0.1s$ to the first post-bleach time point when fitting fluorescence recovery curves. The validity of the fitting was verified by measuring the translational diffusion constant of GFP and CMFDA and comparing these to previously published values.

Data processing, curve fitting and statistical analysis. Indentation and force-relaxation curves collected by AFM were analysed using custom written code in Matlab (Mathworks Inc). Data points where the indentation depth δ was larger than 25% of cell height were excluded. Goodness of fit was evaluated by calculating r^2 values and for analyses only fits with $r^2 > 0.85$ were considered (representing more than 90% of the collected data). The calculated value for each group of variables is presented in terms of mean value and standard deviation (Mean \pm SD). To test pairwise differences in population experiments, Student's t-test was performed between individual treatments. Values of $p < 0.01$ compared to control were considered significant and are indicated by asterisks in the graphs.

RESULTS

Effects of finite cell height. To extract the poroelastic diffusion constant from experimental data, we utilised the finite-element approximation derived by Hu et al.²². In this study, the thickness of the poroelastic material was assumed to be infinite. At short times after the start of relaxation, the infinite half-space solution is applicable for materials of finite thickness. To investigate the precision of short time-scale approximations, we made the simplifying assumption that to the first order indentation can be considered analogous to a one dimensional consolidation. With this assumption, sudden application of a surface stress σ_0 gives rise to the following displacement fields in a finite domain of length h and in an infinite half-space respectively^{1,21}:

$$u(x, t) = \sigma_0 \frac{(1 - 2\nu_s)L}{2G_s(1 - \nu_s)} \sum_{n=1,3,\dots}^{\infty} \frac{8}{n^2\pi^2} \cos \frac{n\pi x}{2h} \left[1 - \exp\left(-n^2\pi^2 \frac{D_p t}{4h^2}\right) \right], \quad (13)$$

$$u(x, t) = \sigma_0 \frac{(1 - 2\nu_s)}{2G_s(1 - \nu_s)} \left[2\sqrt{\frac{Dt}{\pi}} e^{-\frac{x^2}{4D_p t}} - \text{erfc}\left(\frac{x}{2\sqrt{D_p t}}\right) \right]. \quad (14)$$

We utilise these exact solutions to investigate the time-scales over which we can employ the half-space approximation in a material of finite thickness. In our experiments, application of $F \sim 6$ nN via a spherical tip of radius $R = 7.5$ μm resulted in indentation depths of $\delta_0 \sim 1$ μm leading to average stresses of $\sigma_{ave} = F / \pi R \delta \sim 250$ Pa. Fig. S10A-I shows the surface displacements as a function of time for various cell thicknesses (from $h = 2$ to 8 μm) compared to the displacements in an infinite half-space. Comparing the finite and infinite thickness solutions, we find that for cell thicknesses of $h \sim 5$ μm (comparable to our experimental measurements of the height of HeLa cells) the infinite half-space solution is a good approximation for times shorter than 0.5s (less than 15% error, Fig. S10A-II). Hence, fitting our experimental data for time-scales shorter than 0.5s with the infinite half-space solution provides an acceptable approximation.

Recently, detailed finite-element simulations of indentation of thin layers of poroelastic materials²⁰ have shown that force-relaxation can be approximated in terms of stretched exponential functions: $[F(t) - F_f] / [F_i - F_f] = \exp(-\alpha t^\beta)$ where α and β are functions estimated empirically from the simulations that depend on the characteristic length of the problem $L = \sqrt{R\delta}$ and the height h of the layer:

$$\begin{aligned} \alpha &= 1.15 + 0.44(\sqrt{R\delta} / h) + 0.89(\sqrt{R\delta} / h)^2 - 0.42(\sqrt{R\delta} / h)^3 + 0.06(\sqrt{R\delta} / h)^4 \\ \beta &= 0.56 + 0.25(\sqrt{R\delta} / h) + 0.28(\sqrt{R\delta} / h)^2 - 0.31(\sqrt{R\delta} / h)^3 + 0.1(\sqrt{R\delta} / h)^4 - 0.01(\sqrt{R\delta} / h)^5. \end{aligned} \quad (15)$$

In our experiments, we measured a height $h \sim 4.5$ μm for HeLa cells and estimated α and β from the above equations. Fitting experimental force curves with the proposed stretched exponential function indicated that for $h > 4.5$ μm and $\delta < 1.4$ μm , approximating the cell to an infinite half-plane resulted in a less than 25% overestimation of the poroelastic diffusion constant D_p (Fig. S10B).

Rescaling of relaxation curves. To gain further insight into the nature of cellular force-relaxation at short time-scales, we acquired experimental relaxation curves following indentations with increasing depths. To analyse these experiments, we selected cells with identical elasticities such that application of a chosen target force resulted in identical indentation depths and we averaged their relaxation curves. This filtering procedure ensured that the cellular relaxation curves were comparable in all aspects (Fig. S1A, S2A) and allowed us to assess whether or not cellular relaxation was dependent upon indentation depth. Indeed, one hallmark of poroelastic materials is that their characteristic relaxation time is length-scale dependent in contrast to power law relaxations of the form $(F(t) \sim F_0(t/t_0)^\beta)$ and exponential relaxations of the form $(F(t) \sim F_0 \exp(-t/\tau))$ with β and τ indentation depth independent parameters. For ideal stress-relaxations of any power-law or linear viscoelastic material, normalisation of force between any arbitrarily chosen times t_1 and t_2 $[F(t) - F(t_1)] / [F(t_2) - F(t_1)]$ should lead to

collapse of all experimental relaxation curves onto one master curve. After force normalisation, experimental force-relaxation curves acquired on cells for different indentation depths collapsed for times longer than ~ 1 s but were significantly different from one another for shorter times (Fig. S1B-C for MDCK cells and Fig. S2B for HeLa cells), suggesting that, at short times, relaxation is length-scale dependent consistent with a poroelastic behaviour.

Next, we considered the indentation of well-characterised poroelastic materials and examined if, at short times, force-relaxation curves collapse onto one master curve following normalisation of force and rescaling of time with respect to indentation depth (t/δ). To assess this, experimental curves must first be normalised such that force relaxes between 1 and 0 using

$$\frac{F(t) - F(t = t^*)}{F(t = 0) - F(t = t^*)} \quad (16)$$

and then time must be rescaled with respect to indentation depth (t/δ). For physical hydrogels, all experimental force-relaxation curves reach a plateau (F_∞) after $t=t_\infty$ (Fig. S3A) and thus any time $t^*>t_\infty$ is a suitable choice for the normalisation of force (Fig. S3E). Subsequent rescaling of time with respect to indentation depth (t/δ) leads to collapse of all experimental curves onto one master curve (Fig. S3F). To obtain collapse onto a master curve for $t^*<t_\infty$, t^* must be selected proportional to the indentation depth δ specific to each curve: $t^*=\alpha\delta$ where α (with unit of $\text{s}\cdot\mu\text{m}^{-1}$) is an arbitrary number fixed for all curves (Fig. S3C,D).

For cells, experimental force-relaxation curves do not reach a plateau because relaxation follows a power law at long time-scales (Fig. 1D-II). Hence, to determine if relaxation displayed a poroelastic behaviour at short time-scales, we followed the force normalisation and time rescaling steps described above for cases where $t^*<t_\infty$. These procedures resulted in all cellular force-relaxation curves collapsing onto a single master curve (Fig. S1E, Fig. S2D). This behaviour was apparent in poroelastic hydrogels for both long and short time-scales (Fig. S3D,F) and in cells for times shorter than ~ 0.5 s (Fig. S1E, Fig. S2D). Taken together, these data suggested that at short time-scales cellular relaxation is indentation depth dependent and therefore that cells behaved as poroelastic materials.

Apparent viscosity of the cytoplasm. To measure the apparent viscosity of the cytoplasm, we fitted force-relaxation curves with $(F(t)\sim e^{-k_1 t/\eta})$. Using the approach phase of AFM indentation curves we can measure cellular elasticity and therefore the relaxations predicted by a viscoelastic formulation depend on only one free parameter: the apparent viscosity η . Viscoelastic formulations were found to replicate experimental force-relaxation curves well (on average $r^2=0.92$), but the early phase of force-relaxation was fit somewhat less accurately by viscoelastic models (gray line, Fig. S4A) compared to poroelastic fits (black line, Fig. S4A). Indeed, viscoelastic models gave rise to somewhat larger errors than poroelastic models (Fig. S4A). For HeLa cells, we measured an average apparent viscosity of $\eta=166\pm 81$ Pa.s. For HT1080 cells, we found an apparent viscosity $\eta=77\pm 37$ Pa.s, and for MDCK cells, $\eta=50\pm 15$ Pa.s.

Estimation of the hydraulic pore size from experimental measurements of D_p . Using equations (7) and (8) together with our experimental measurements of D_p ($\sim 40\mu\text{m}^2\cdot\text{s}^{-1}$), E (~ 1 kPa), v_s (~ 0.3), and the fluid fraction ϕ (~ 0.75), we can estimate the hydraulic pore size numerically assuming $\kappa\sim 4$, its lower bound for a random distribution of particulate spheres for $\phi\sim 0.75$ ³¹. These values yield an estimate of ~ 0.05 for α in isotonic conditions. Multiple experimental reports have shown that for small molecules the viscosity μ of the fluid-phase of cytoplasm (cytosol) is 2-3 fold higher in cells than in aqueous media^{32,33}. Using these values in equation (7) yields a hydraulic pore size ξ of ~ 15 nm, comparable to the hydrodynamic radius of qdots with their PEG-passivation layer³⁴.

Effective bleach radius in FRAP experiments. To derive quantitative measurements of the translational diffusion constants of molecules within the cytoplasm using the methods described in²⁸, we experimentally determined the effective bleach radius for a nominal bleaching zone of diameter $0.5\mu\text{m}$ in the first post-bleach image (Fig. S8A-III). Averaging over all diameters passing through the centre of the nominal bleach regions

yielded an experimental curve that could be fit with equation (11) to find $r_e=1.5\pm0.2$ μm (S5A-V, $N=6$ measurements on $n=6$ cells).

Measurement of translational diffusion constants in cells. Using the analytical procedures described in supplementary methods, the estimated translational diffusion constant for CMFDA was $D_{T, \text{CMFDA}}=38.3\pm8$ $\mu\text{m}^2.\text{s}^{-1}$ ($N=19$ measurements on $n=7$ cells) in good agreement with published values in cells (Fig. 3B, $D_T=24\text{--}40$ $\mu\text{m}^2.\text{s}^{-1}$,³⁵) and 6 fold slower than in aqueous conditions ($D_{T, \text{CMFDA, aqueous}}=240$ $\mu\text{m}^2.\text{s}^{-1}$ ³⁵) also consistent with previous reports³⁵. For GFP freely diffusing in the cytoplasm, we found $D_{T, \text{GFP}}=24.9\pm7$ $\mu\text{m}^2.\text{s}^{-1}$ (Fig. S8B, $N=18$ measurements on $n=7$ cells), consistent with values reported by others²⁸. It should be noted that with CMFDA loss of fluorescence due to imaging is very high (also reported by others, Fig. 3B). Therefore, we only utilised data points up to a total fluorescence loss of 15% due to imaging to estimate the translational diffusion of fluorophores in cells in normal isotonic condition. To estimate the reduction in translational diffusion of CMFDA in cells under hyperosmotic conditions, we normalised the data following the procedures described in³⁶ and this gave an estimated $D_{T, \text{CMFDA, Hyper}}=14$ $\mu\text{m}^2.\text{s}^{-1}$ ($N=20$ measurements on $n=5$ cells) ~ 3 fold lower than in isoosmotic conditions.

Table S1 Effects of osmotic perturbations on translational diffusion coefficients D_T ($\mu\text{m}^2.\text{s}^{-1}$)

CMFDA-Control $N=19, n=7$	CMFDA-PEG-400 $N=20, n=5$	EGFP10x-Control $N=17, n=6$	EGFP10x-Water+N+D $N=23, n=7$
38.3 \pm 8	13.7 \pm 4	8.6 \pm 2	15.5 \pm 5

Estimation of cortical F-actin turnover half-time. To assess the turnover rate of the F-actin cytoskeleton, HeLa cells stably expressing actin-GFP were blocked in prometaphase by overnight treatment with 100 nM nocodazole. Under these conditions, cells form a well-defined actin cortex. To estimate F-actin turnover, photobleaching was performed on the F-actin cortex and recovery was imaged at a frame rate of 0.9s/frame (Fig. S8C). We obtained a half time recovery of $t_{1/2, \text{F-actin}}=11.2\pm3$ s ($N=10$ measurements on $n=4$ cells).

Spatial variations in poroelastic properties. Maps of cellular elasticity measured by AFM show that E is strongly dependent upon location within the cell with actin-rich organelles (lamellipodium, actin stress fibres) appearing significantly stiffer than other parts of the cell³⁷. Hence, we asked if something similar could be observed for poroelastic properties by measuring these at different locations along the cell long axis (Fig. S9A). We performed $N=386$ total measurements on $n=30$ cells and displayed the measurements averaged over 2 μm bins as a function of distance to the centroid of the nucleus. Cell height decreased significantly with increasing distance from the nucleus (Fig. S9B) and this measurement enabled us to exclude low areas of the cell that are prone to measurement artefacts due to limited thickness. The poroelastic diffusion constant D_p decreased slightly, but not significantly, away from the nucleus decreasing from 40 $\mu\text{m}^2.\text{s}^{-1}$ to ~ 30 $\mu\text{m}^2.\text{s}^{-1}$ ($p>0.02$, Fig. S9D). In contrast, elasticity increased significantly away from the nucleus increasing from ~ 500 Pa to ~ 1200 Pa in lower areas (Fig. S9C). Finally, the lumped pore size estimated from the ratio $(D_p\mu/E)^{1/2}$ also decreased significantly away from the nucleus (Fig. S9E).

DISCUSSION

A length-scale dependent effective cellular viscosity. At time-scales short compared to 1s, force-relaxation decays exponentially in poroelastic models as it does in simple Maxwell models of the cytoplasm (Supplementary Results), but with the important difference that the Maxwell model makes no distinction between shear and dilatation, and has no microstructural basis in terms of the two phase picture of a fluid bathed network. However, in the context of observations past and present, this does suggest the following relationship for a length-scale dependent effective cellular viscosity η

$$\eta \sim \mu \left(\frac{L}{\xi} \right)^2, \quad (17)$$

with L a characteristic length-scale and μ the viscosity of cytosol. Given the dependence of η on the ratio of a mesoscopic length-scale to a microscopic length-scale in the system may explain the large spread in reported measurements of cytoplasmic viscosities^{38,39}.

Poroelasticity in physiological cell shape changes and tissue deformations. To gain an understanding of how widespread poroelastic effects are in the rheology of isolated cells and cells within tissues, one can compute the poroelastic Péclet number $Pe = (VL)/D_p$, with V a characteristic velocity (due to active movement, external loading, etc). For $Pe \gg 1$, poroelastic effects dominate the viscoelastic response of the cytoplasm to shape change due to externally applied loading or intrinsic cellular forces. In isolated cells, poroelastic effects have been implicated in the formation of protrusions such as lamellipodia or blebs⁴⁰. For these, the rate of protrusion growth can be chosen as a characteristic velocity. In rapidly moving cells, forward-directed intracellular water flows^{41,42} resulting from pressure gradients due to myosin contraction of the cell rear have been proposed to participate in lamellipodial protrusion⁴². Assuming a representative lamellipodium length of $L \sim 10 \mu\text{m}$ and protrusion velocities of $V \sim 0.3 \mu\text{m.s}^{-1}$, poroelastic effects will play an important role if $D_p \leq 3 \mu\text{m}^2.\text{s}^{-1}$, lower than measured in the cytoplasm but consistent with the far higher F-actin density observed in electron micrographs of the lamellipodium⁴³. Furthermore, cells can also migrate using blebbing motility⁴⁴ where large quasi-spherical blebs ($L \sim 10 \mu\text{m}$) arise at the cell front with protrusion rates of $V \sim 1 \mu\text{m.s}^{-1}$ giving an estimate of $D_p \sim 10 \mu\text{m}^2.\text{s}^{-1}$ (comparable to the values reported here) to obtain $Pe \geq 1$. During normal physiological function, cells within tissues of the respiratory and cardiovascular systems are subjected to strains $\epsilon > 20\%$ applied at strain rates $\epsilon_t > 20\%.\text{s}^{-1}$. As a first approximation, we assume that these cells, with a representative length L_{cell} , undergo a length change $L \sim \epsilon L_{cell}$ applied with a characteristic velocity $V \sim L_{cell}\epsilon_t$. For cells within the lung alveola⁴⁵, $L_{cell} \sim 30 \mu\text{m}$, $\epsilon \sim 20\%$, $\epsilon_t \sim 20\%.\text{s}^{-1}$ and assuming $D_p \sim 10 \mu\text{m}^2.\text{s}^{-1}$ (based on our measurements), we find $Pe \sim 3$. Hence, these simple estimates of Pe suggest that water redistribution participates in setting the rheology of cells within tissues under normal physiological conditions.

References:

- 1 Detournay, E. & Cheng, A. H. D. Fundamentals of poroelasticity. *Comprehensive rock engineering* **2**, 113-171 (1993).
- 2 Biot, M. A. General theory of three-dimensional consolidation. *Journal of applied physics* **12**, 155 (1941).
- 3 Mow, V. C., Kuei, S. C., Lai, W. M. & Armstrong, C. G. Biphasic creep and stress relaxation of articular cartilage in compression: theory and experiments. *Journal of biomechanical engineering* **102**, 73 (1980).
- 4 Scheidegger, A. E. The physics of flow through porous media. *Soil Science* **86**, 355 (1958).
- 5 Ory, D. S., Neugeboren, B. A. & Mulligan, R. C. A stable human-derived packaging cell line for production of high titer retrovirus/vesicular stomatitis virus G pseudotypes. *Proceedings of the National Academy of Sciences of the United States of America* **93**, 11400 (1996).
- 6 Riedl, J. *et al.* Lifeact: a versatile marker to visualize F-actin. *Nature methods* **5**, 605-607 (2008).
- 7 Bancaud, A. *et al.* Molecular crowding affects diffusion and binding of nuclear proteins in heterochromatin and reveals the fractal organization of chromatin. *The EMBO journal* **28**, 3785-3798 (2009).
- 8 Moulding, D. A. *et al.* Unregulated actin polymerization by WASp causes defects of mitosis and cytokinesis in X-linked neutropenia. *The Journal of experimental medicine* **204**, 2213 (2007).
- 9 Demaison, C. *et al.* High-level transduction and gene expression in hematopoietic repopulating cells using a human immunodeficiency virus type 1-based lentiviral vector containing an internal spleen focus forming virus promoter. *Human gene therapy* **13**, 803-813 (2002).
- 10 Zheng, Y., Wong, M. L., Alberts, B. & Mitchison, T. Nucleation of microtubule assembly by a gamma-tubulin-containing ring complex. *Nature* **378**, 578-583 (1995).
- 11 Keppler, A. & Ellenberg, J. Chromophore-assisted laser inactivation of α - and β -tubulin SNAP-tag fusion proteins inside living cells. *ACS Chemical Biology* **4**, 127-138 (2009).
- 12 Werner, N. S. *et al.* Epidermolysis bullosa simplex-type mutations alter the dynamics of the keratin cytoskeleton and reveal a contribution of actin to the transport of keratin subunits. *Molecular biology of the cell* **15**, 990 (2004).
- 13 Zhou, E. H. *et al.* Universal behavior of the osmotically compressed cell and its analogy to the colloidal glass transition. *Proceedings of the National Academy of Sciences* **106**, 10632 (2009).
- 14 Hoffmann, E. K., Lambert, I. H. & Pedersen, S. F. Physiology of cell volume regulation in vertebrates. *Physiological reviews* **89**, 193 (2009).
- 15 Lin, D. C., Dimitriadis, E. K. & Horkay, F. Robust strategies for automated AFM force curve analysis—I. Non-adhesive indentation of soft, inhomogeneous materials. *Journal of biomechanical engineering* **129**, 430 (2007).
- 16 Harris, A. R. & Charras, G. Experimental validation of atomic force microscopy-based cell elasticity measurements. *Nanotechnology* **22**, 345102 (2011).
- 17 Johnson, K. L. *Contact mechanics*. (Cambridge university press, 1987).
- 18 Dimitriadis, E. K., Horkay, F., Maresca, J., Kachar, B. & Chadwick, R. S. Determination of elastic moduli of thin layers of soft material using the atomic force microscope. *Biophysical Journal* **82**, 2798-2810 (2002).
- 19 Charras, G. T., Lehenkari, P. P. & Horton, M. A. Atomic force microscopy can be used to mechanically stimulate osteoblasts and evaluate cellular strain distributions. *Ultramicroscopy* **86**, 85-95 (2001).
- 20 Chan, E. P., Hu, Y., Johnson, P. M., Suo, Z. & Stafford, C. M. Spherical indentation testing of poroelastic relaxations in thin hydrogel layers. *Soft Matter* **8**, 1492-1498 (2012).
- 21 Wang, H. *Theory of linear poroelasticity: with applications to geomechanics and hydrogeology*. (Princeton Univ Pr, 2000).
- 22 Hu, Y., Zhao, X., Vlassak, J. J. & Suo, Z. Using indentation to characterize the poroelasticity of gels. *Applied Physics Letters* **96**, 121904 (2010).
- 23 Galli, M., Oyen, M. L. & Source, C. Fast Identification of Poroelastic Parameters from Indentation Tests. *Computer Modeling in Engineering and Science* **48**, 241-270 (2009).
- 24 Charras, G. T., Mitchison, T. J. & Mahadevan, L. Animal cell hydraulics. *Journal of Cell Science* **122**, 3233 (2009).

- 25 Mitchison, T. J., Charras, G. T. & Mahadevan, L. 215-223 (Elsevier).
- 26 Darling, E. M., Zauscher, S. & Guilak, F. Viscoelastic properties of zonal articular chondrocytes measured by atomic force microscopy. *Osteoarthritis and Cartilage* **14**, 571-579 (2006).
- 27 Charras, G. T., Hu, C. K., Coughlin, M. & Mitchison, T. J. Reassembly of contractile actin cortex in cell blebs. *The Journal of cell biology* **175**, 477-490 (2006).
- 28 Kang, M., Day, C. A., Drake, K., Kenworthy, A. K. & DiBenedetto, E. A generalization of theory for two-dimensional fluorescence recovery after photobleaching applicable to confocal laser scanning microscopes. *Biophysical Journal* **97**, 1501-1511 (2009).
- 29 Axelrod, D., Koppel, D. E., Schlessinger, J., Elson, E. & Webb, W. W. Mobility measurement by analysis of fluorescence photobleaching recovery kinetics. *Biophysical Journal* **16**, 1055-1069 (1976).
- 30 Soumpasis, D. M. Theoretical analysis of fluorescence photobleaching recovery experiments. *Biophysical Journal* **41**, 95-97 (1983).
- 31 Happel, J. & Brenner, H. *Low Reynolds number hydrodynamics: with special applications to particulate media*. Vol. 1 (Springer, 1983).
- 32 Mastro, A. M., Babich, M. A., Taylor, W. D. & Keith, A. D. Diffusion of a small molecule in the cytoplasm of mammalian cells. *Proceedings of the National Academy of Sciences* **81**, 3414 (1984).
- 33 Persson, E. & Halle, B. Cell water dynamics on multiple time scales. *Proceedings of the National Academy of Sciences* **105**, 6266 (2008).
- 34 Derfus, A. M., Chan, W. C. W. & Bhatia, S. N. Intracellular delivery of quantum dots for live cell labeling and organelle tracking. *Advanced Materials* **16**, 961-966 (2004).
- 35 Swaminathan, R., Bicknese, S., Periasamy, N. & Verkman, A. S. Cytoplasmic viscosity near the cell plasma membrane. *Biophysical Journal* **71**, 1140-1151 (1996).
- 36 Phair, R. D. & Misteli, T. High mobility of proteins in the mammalian cell nucleus. *Nature* **404**, 604-608 (2000).
- 37 Rotsch, C. & Radmacher, M. Drug-induced changes of cytoskeletal structure and mechanics in fibroblasts: an atomic force microscopy study. *Biophys J* **78**, 520-535 (2000).
- 38 Bausch, A. R., Möller, W. & Sackmann, E. Measurement of local viscoelasticity and forces in living cells by magnetic tweezers. *Biophysical journal* **76**, 573-579 (1999).
- 39 Hoffman, B. D. & Crocker, J. C. Cell mechanics: dissecting the physical responses of cells to force. *Annual review of biomedical engineering* **11**, 259-288 (2009).
- 40 Charras, G. T., Yarrow, J. C., Horton, M. A., Mahadevan, L. & Mitchison, T. J. Non-equilibration of hydrostatic pressure in blebbing cells. *Nature* **435**, 365-369 (2005).
- 41 Zicha, D. *et al.* Rapid actin transport during cell protrusion. *Science* **300**, 142-145 (2003).
- 42 Keren, K., Yam, P. T., Kinkhabwala, A., Mogilner, A. & Theriot, J. A. Intracellular fluid flow in rapidly moving cells. *Nature cell biology* **11**, 1219-1224 (2009).
- 43 Pollard, T. D. & Borisy, G. G. Cellular motility driven by assembly and disassembly of actin filaments. *Cell* **112**, 453-465 (2003).
- 44 Charras, G. & Paluch, E. Blebs lead the way: how to migrate without lamellipodia. *Nature Reviews Molecular Cell Biology* **9**, 730-736 (2008).
- 45 Perlman, C. E. & Bhattacharya, J. Alveolar expansion imaged by optical sectioning microscopy. *Journal of applied physiology* **103**, 1037-1044 (2007).

SUPPLEMENTARY MOVIE

Movement of PEG-passivated quantum dots microinjected in a HeLa cell in isoosmotic conditions (left) and in hyperosmotic conditions (right). Both movies are 120 frames long totalling 18 s and are single confocal sections. In isoosmotic conditions, quantum dots move freely (left); whereas in hyperosmotic conditions, quantum dots are immobile because they are trapped within the cytoplasmic mesh (right). Scale bars =10 μm .

SUPPLEMENTARY FIGURES

Figure S1

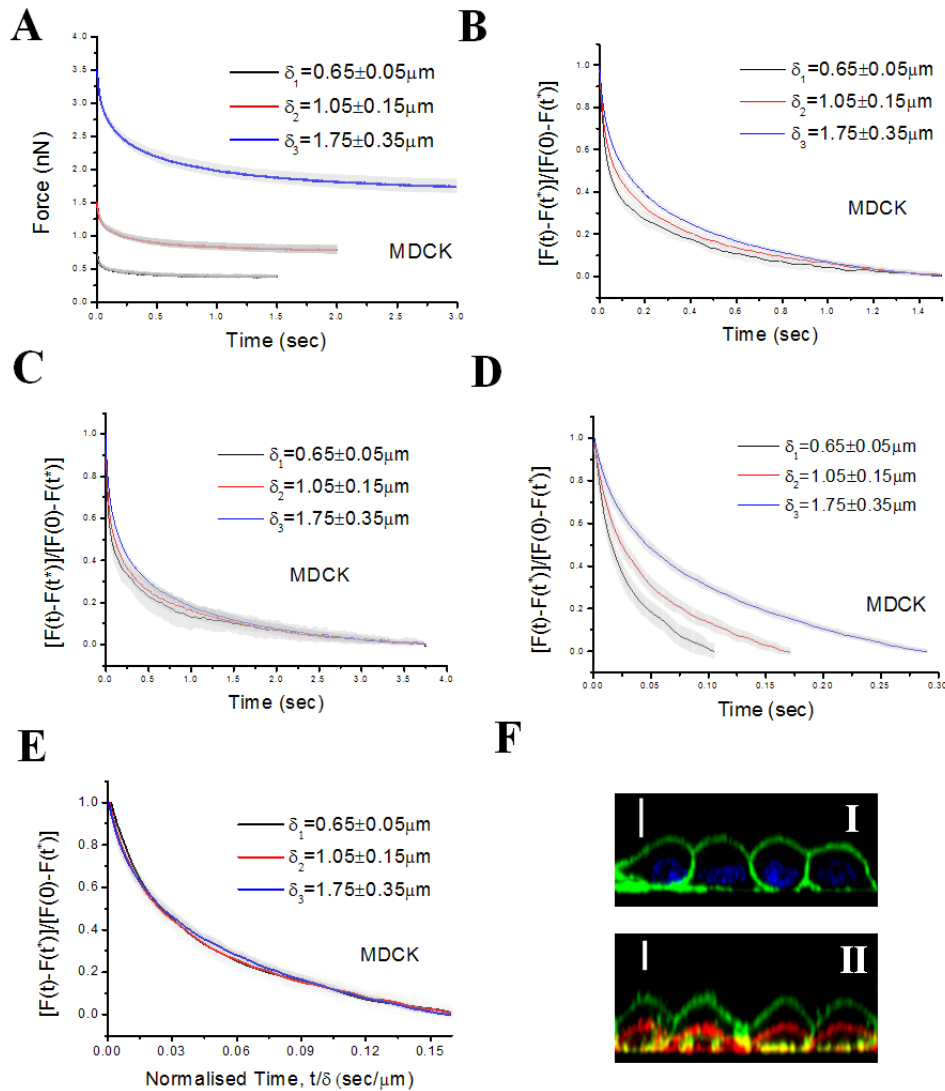


FIGURE S1 In all graphs, solid lines and grey shadings represent the mean and standard deviations at each data point, respectively. (A) Force-relaxation curves acquired on MDCK cells for three different indentation depths (δ_1 , δ_2 and δ_3). Each relaxation curve is the average of 20 force-relaxation curves acquired on cells with matching elasticities of $E = 0.4 \pm 0.1$ kPa. Elasticity matching ensured that identical forces were applied onto each cell to obtain a given indentation depth. (B) Normalisation of force-relaxation curves shown in A using equation (16) choosing $t^* = 1.5$ s for all curves. Relaxation curves were significantly different from one another for times shorter than ~ 0.5 s but appeared to collapse at times longer than ~ 1.2 s. (C) Normalisation of force-relaxation curves shown in A using equation (16) choosing $t^* = 3.6$ s for all curves. Relaxation curves collapsed for times longer than ~ 1.2 s. (D) Normalisation of force-relaxation curves shown in A using equation (16) plotted as a function of time. For force renormalisation, a separate time t^* dependent on indentation depth was chosen for each curve with $t^* = \alpha\delta$. Choosing $\alpha = 0.16$ s. μm^{-1} gave times $t_1^* \sim 105$ ms, $t_2^* \sim 170$ ms and $t_3^* \sim 285$ ms. (E) Normalised force-relaxation curves from D plotted as a function of time divided by indentation depth δ (t/δ). Time rescaling was performed for each force relaxation curve separately using their respective indentation depth δ . Following force renormalisation and time-rescaling, all three force-relaxation curves collapsed onto one single curve. (F) (I) zx section of MDCK cells expressing a membrane marker (PH-PLC δ , green) and stained for nucleic acids with Hoechst 34332 (blue). Nuclei localised to the basal side of cells far from the apex. Scale bar = 10 μm . (II) zx profile of MDCK cells before (green) and after (red) application of 500 mM sucrose. Cell height decreased significantly in response to increase in medium osmolarity.

Figure S2

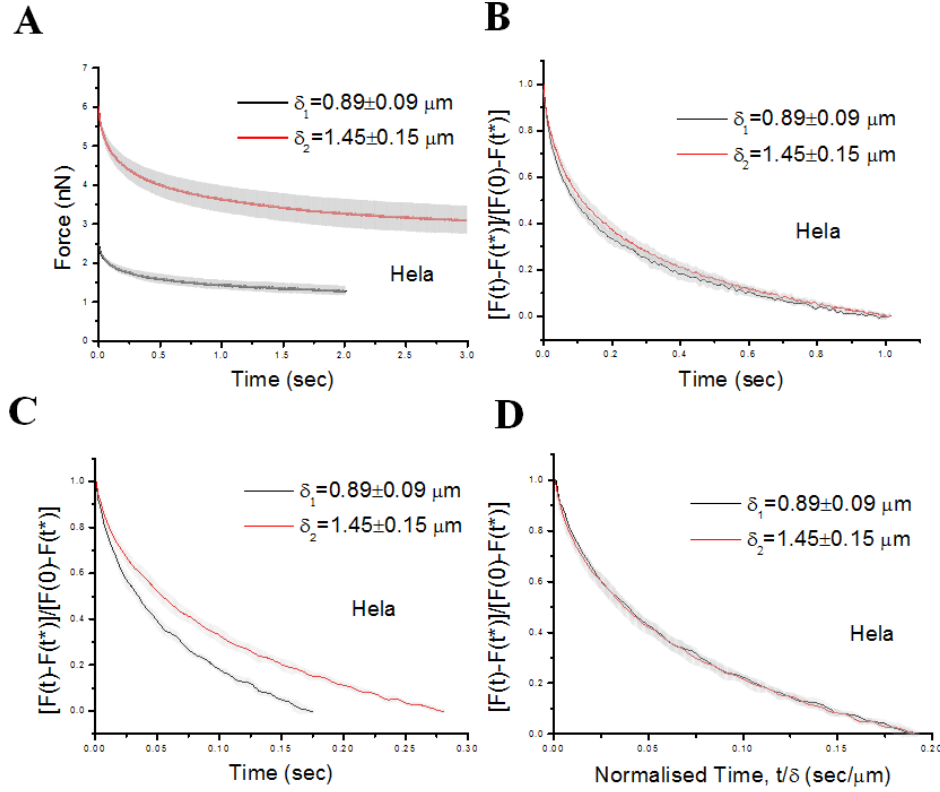


FIGURE S2 In all graphs, solid lines and grey shadings represent the mean and standard deviations at each data point, respectively. (A) Force-relaxation curves acquired on HeLa cells for two different indentation depths (δ_1 and δ_2). Each relaxation curve is the average of 5 force-relaxation curves acquired on cells with matching elasticities of $E=0.66 \pm 0.1$ kPa and heights of $h=5.5 \pm 0.3 \mu\text{m}$. This ensured that identical forces were applied onto each cell to obtain a given indentation depth. Matching of cell heights was necessary to minimise substrate effects due to the smaller thickness of HeLa cells compared to MDCK cells. (B) Normalisation of force-relaxation curves shown in A using equation (16) choosing $t^*=1$ s for all curves. Relaxation curves were significantly different from one another for times shorter than ~ 0.5 s but appeared to collapse at times longer than ~ 0.6 s. (C) Normalisation of force-relaxation curves shown in A using equation (16) plotted as a function of time. For force renormalisation, a separate time t^* dependent on indentation depth was chosen for each curve with $t^*=\alpha\delta$. Choosing $\alpha=0.19 \text{ s} \cdot \mu\text{m}^{-1}$ gave times $t_1^* \sim 170$ ms and $t_2^* \sim 275$ ms. (D) Normalised force-relaxation curves from C plotted as a function of time divided by indentation depth δ (t/δ). Time rescaling was performed for each force relaxation curve separately using their respective indentation depth. Following force renormalisation and time-rescaling, both force-relaxation curves collapsed onto one single curve.

Figure S3

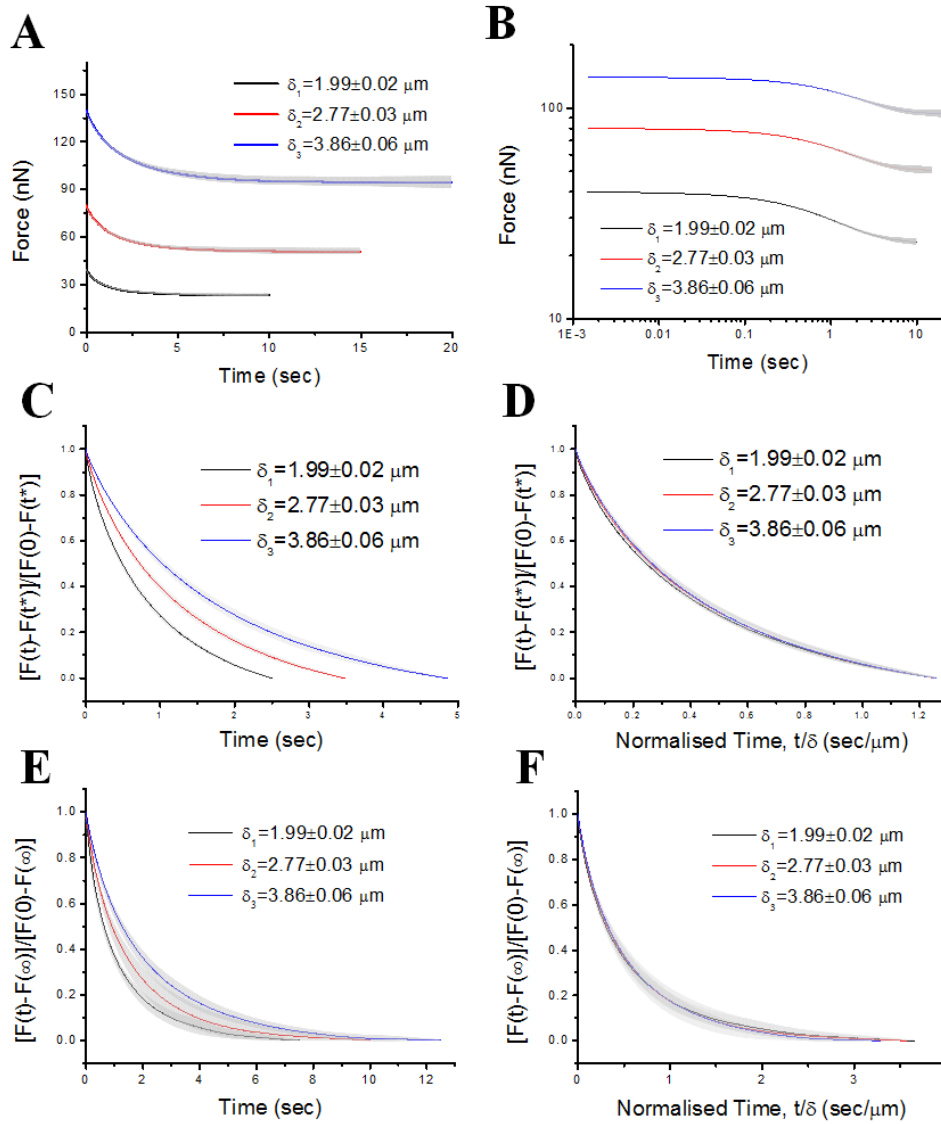


FIGURE S3 In all graphs, solid lines and grey shadings represent the mean and standard deviations at each data point, respectively. (A) Force-relaxation curves acquired on a hydrogel for three different indentation depths (δ_1 , δ_2 and δ_3). Each data point is the average of 20 measurements acquired at different positions on the hydrogel surface. (B) log-log plot of the curves shown in (A). Curves show characteristic plateaus at short and long time-scales. (C) Normalisation of force-relaxation curves shown in A using equation (16) plotted as a function of time. For force renormalisation, a separate time t^* dependent on indentation depth was chosen for each curve with $t^* = \alpha\delta$. Choosing $\alpha = 1.25 \text{ s}\cdot\mu\text{m}^{-1}$ gave times $t_1^* = 2.5 \text{ s}$, $t_2^* = 3.5 \text{ s}$ and $t_3^* = 4.9 \text{ s}$. (D) Normalised force-relaxation curves from C plotted as a function of time divided by indentation depth δ (t/δ). Time rescaling was performed for each force-relaxation curve separately using their respective indentation depth. Following force renormalisation and time-rescaling, all force-relaxation curves collapsed onto one single curve. (E) Normalisation of force-relaxation curves using equation (16) plotted as a function of time. For force renormalisation, a separate time t^* was chosen such that $t^* = t_\infty$, the time at which each curve reaches its plateau: $t_1^* = 7.5 \text{ s}$, $t_2^* = 10 \text{ s}$ and $t_3^* = 12.5 \text{ s}$. (F) Normalised force-relaxation curves from E plotted as a function of time divided by indentation depth δ (t/δ). Time rescaling was performed for each force relaxation curve separately using their respective indentation depth. Following force renormalisation and time-rescaling, all force-relaxation curves collapsed onto one single curve.

Figure S4

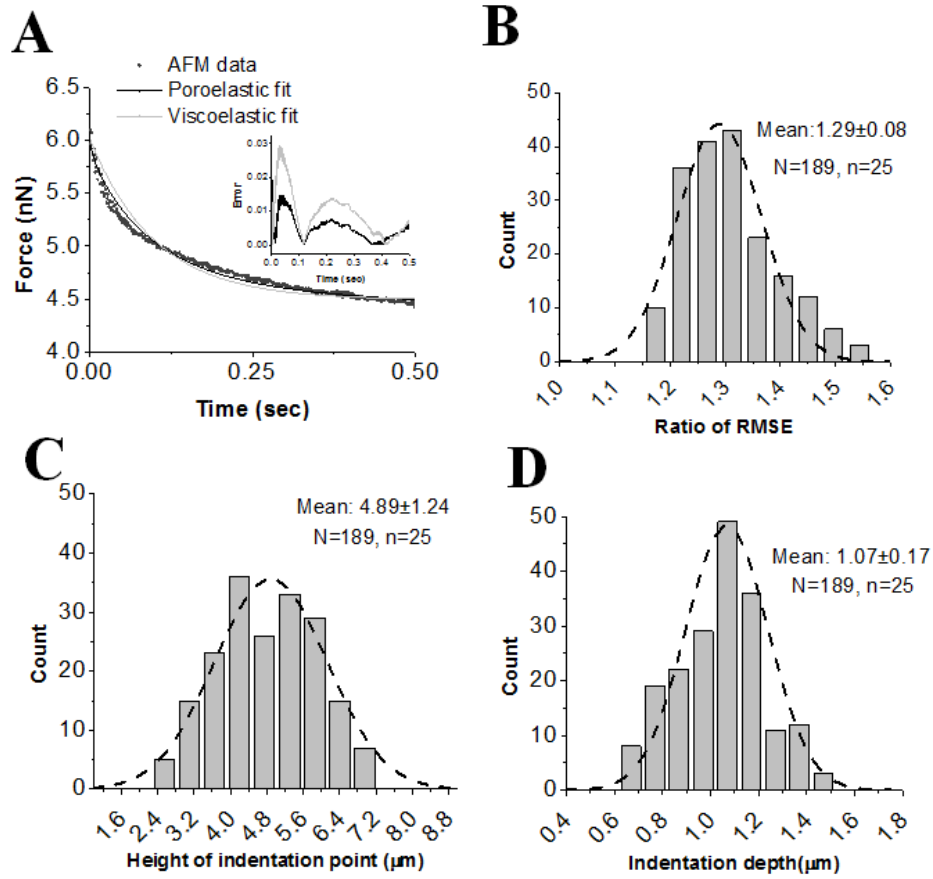


FIGURE S4 All measurements displayed in this graph were effected on HeLa cells. (A) The first 0.5 s of force-relaxation curves were fitted with the poroelastic model (black line) and the standard linear viscoelastic model (grey line). Both models fitted the data well, but poroelastic models were somewhat better than the single phase viscoelastic model at short times. Inset: the percentage error of each fit defined as $|F_{AFM} - F_{fit}|/F_{AFM}$. (B) Ratio of root mean square error (RMSE) of the viscoelastic fit to the RMSE of poroelastic fit. (C) Height of cell at indentation point. (D) Indentation depth. N indicates the number of measurements and n the number of cells.

Figure S5

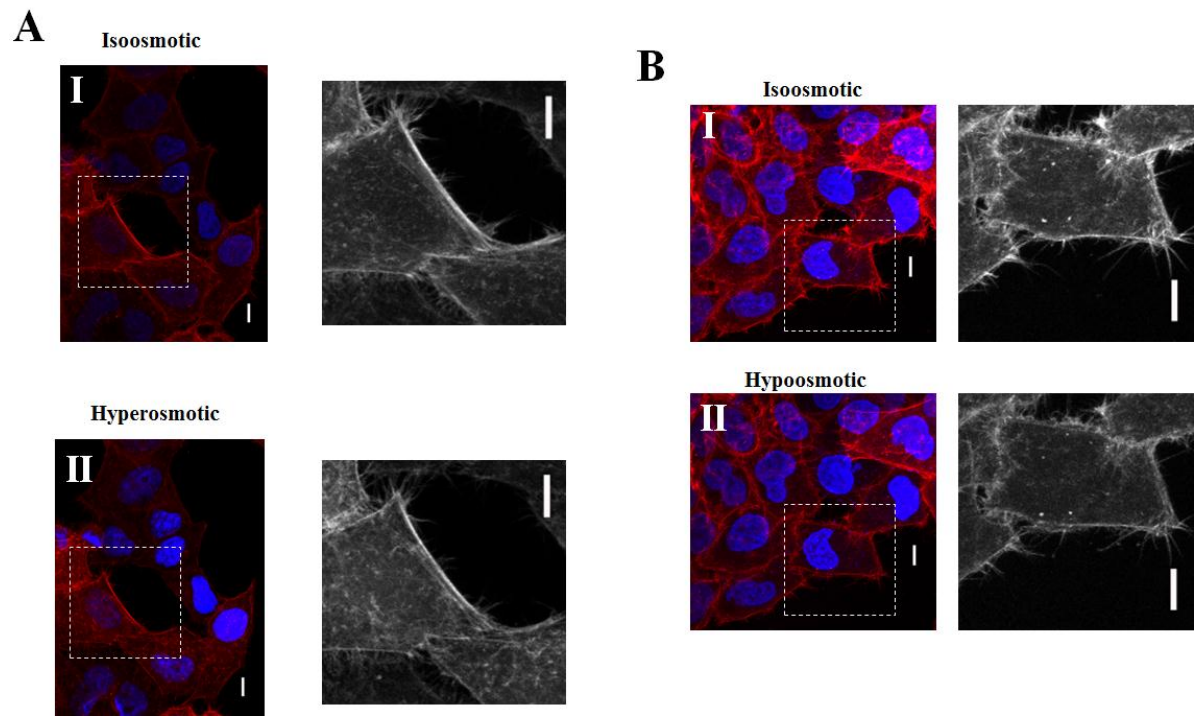


FIGURE S5 The F-actin cytoskeleton does not reorganise in response to hypoosmotic treatment (A) or hyperosmotic treatment (B). All images are maximum projections of a confocal image stack of cells expressing Life-act ruby (red). Nuclei were stained with Hoechst 34332 (blue). In A and B, image (I) shows the cell before addition of osmolyte and image (II) after addition. In A and B, the right hand panels show a magnified region from the left hand panels. Scale bar = 10 μm . No dramatic change in F-actin distribution could be observed after hypoosmotic (A) or hyperosmotic (B) shock.

Figure S6

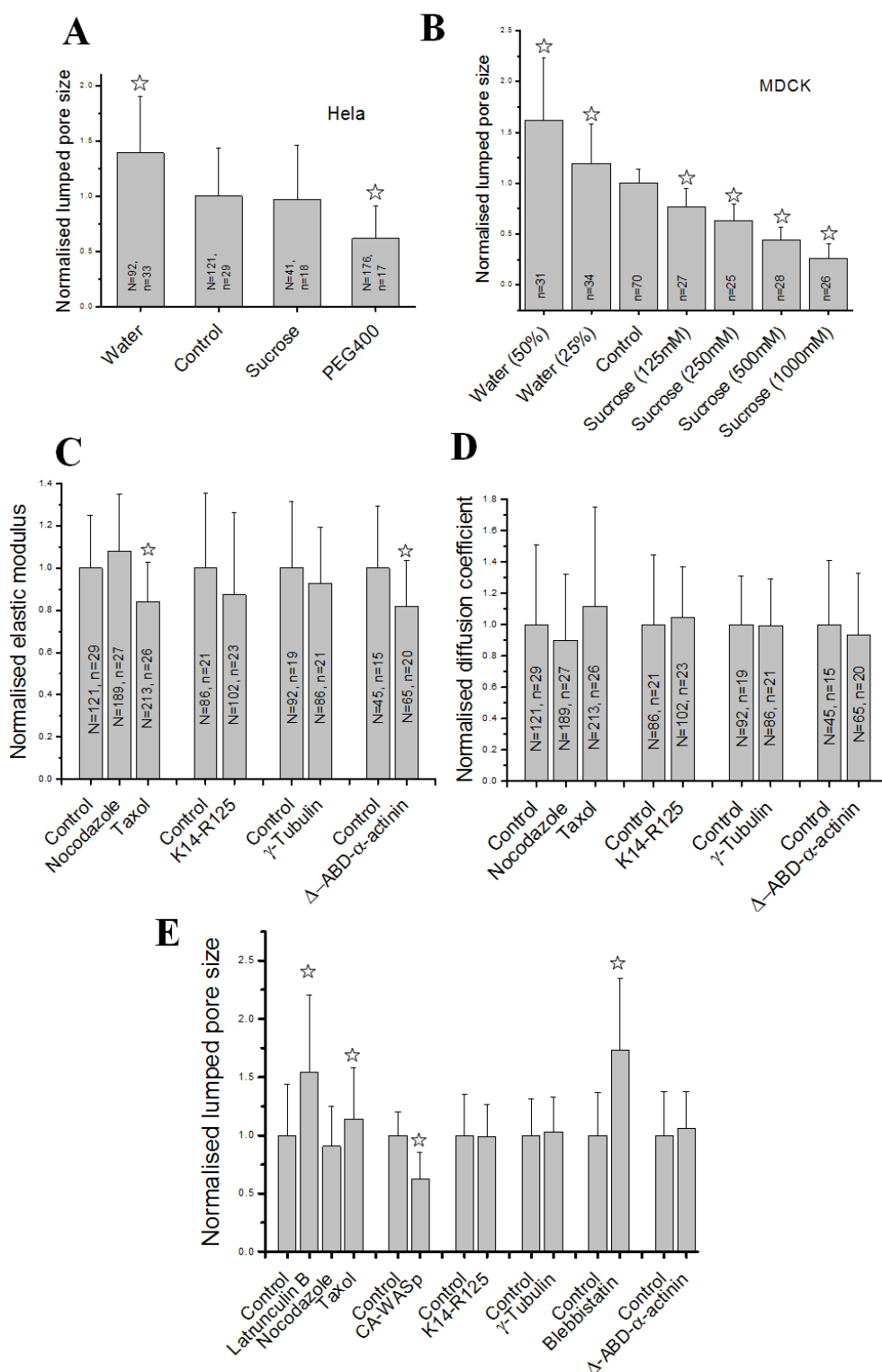


FIGURE S6 (A) Effect of volume changes on the lumped pore size of HeLa cells estimated from the ratio $(D_p\mu/E)^{1/2}$. (B) Effect of volume changes on the lumped pore size of MDCK cells estimated from the ratio $(D_p\mu/E)^{1/2}$. (C-E) Effect of drug treatments and genetic perturbations on the elastic modulus E (C), the poroelastic diffusion constant D_p (D), and the lumped pore size (E) of HeLa cells. The lumped pore size was estimated from the ratio $(D_p\mu/E)^{1/2}$.

Figure S7

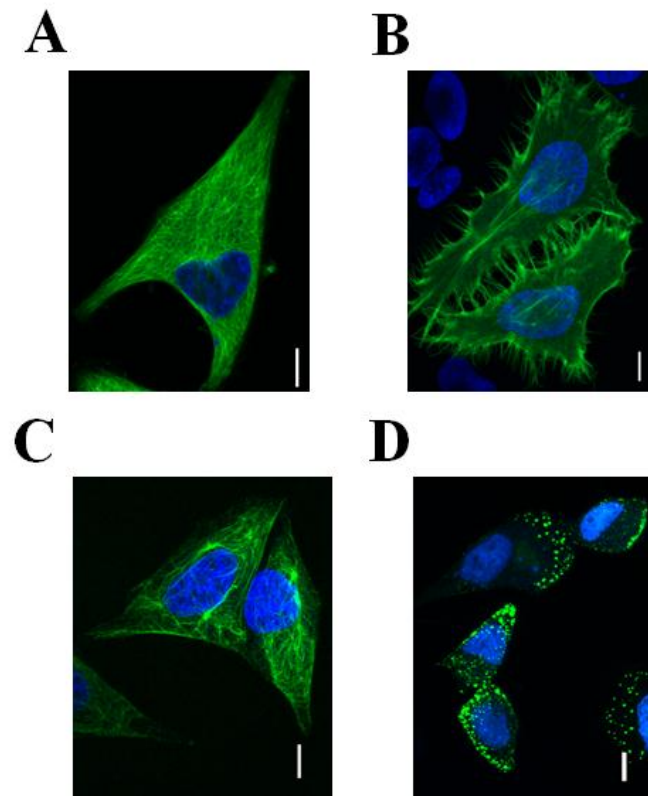


FIGURE S7 Cellular distribution of cytoskeletal fibres. Scale bars =10 μ m. Nuclei are shown in blue and GFP-tagged cytoskeletal fibres are shown in green. (A) Maximum projection of a cell expressing tubulin-GFP. GFP- α -tubulin was homogeneously localised throughout the cell body. (B) Maximum projection of cells expressing Life-act-GFP, an F-actin reporter construct. F-actin was enriched in cell protrusions but was also present in the cell body. (C) Maximum projection of cells expressing keratin18-GFP. Intermediate filaments (keratin 18) were homogeneously distributed throughout the cell body. (D) Overexpression of the dominant mutant Keratin 14 R125C resulted in aggregation of the cellular keratin network.

Figure S8

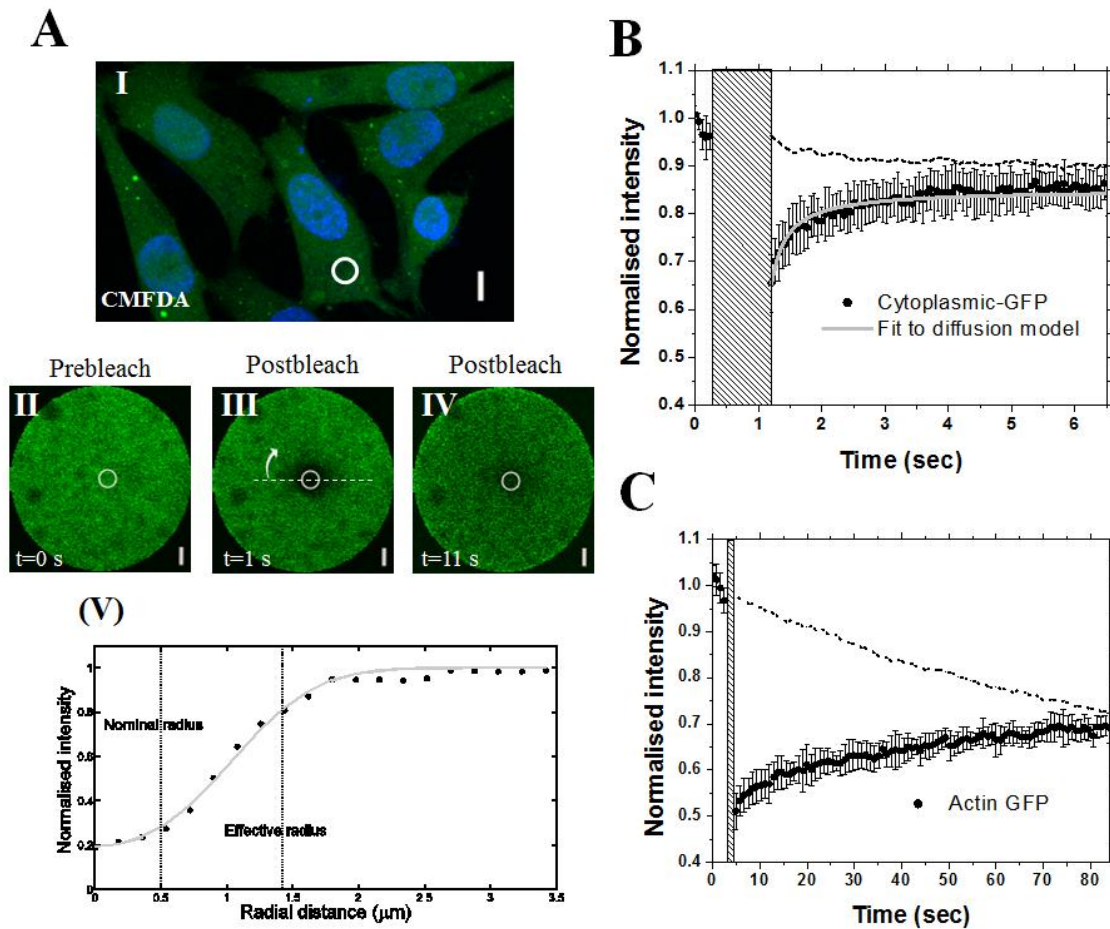
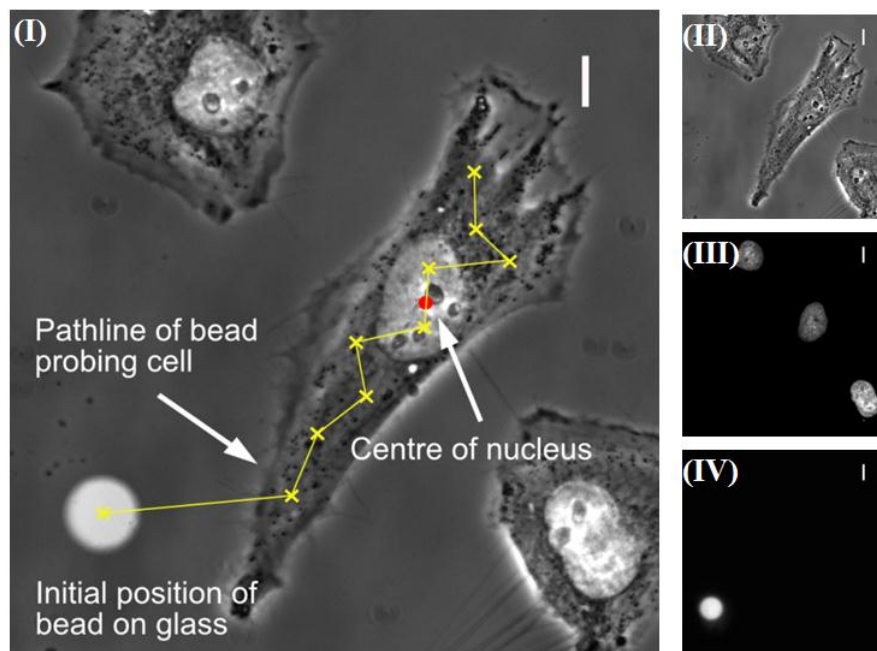


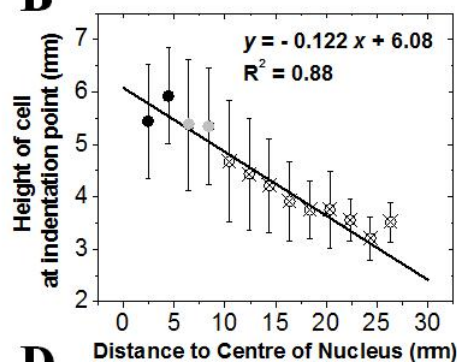
Figure S8 Fluorescence recovery after photobleaching in HeLa cells. (A) (I) Confocal image of cells loaded with the cytoplasmic indicator CMFDA (green). Nuclei (blue) were stained with Hoechst 34332. Scale bar =10 μm . (II-III-IV) Time series of a photobleaching experiment in the cytoplasm of the cells shown in (I, indicated by the white circle). The white circle in images (II-IV) denotes the nominal photobleaching zone. In all three images, scale bars =1 μm . (II) shows the last frame prior to photobleaching. (III) shows the first frame after photobleaching. The bleached region is clearly apparent and larger than the nominal photobleaching zone. (IV) After a long time interval, fluorescence intensity re-homogenises due to diffusion. (V) Fluorescence intensity immediately after photobleaching in the cytoplasm centered on the photobleaching zone in frame (III). Fluorescence was normalised to the intensity far away from the photobleaching zone. In (B) and (C), dashed lines indicate loss of fluorescence due to imaging in a region outside of the zone of FRAP, error bars indicate the standard deviation for each time point, and the greyed area indicates the duration of photobleaching. (B) Fluorescence recovery after photobleaching of monomeric GFP in isosmotic conditions. Solid lines indicate fluorescence recovery after photobleaching and are the average of $N=18$ measurements on $n=7$ cells. The experimental recovery was fitted with the theoretical model described in ²⁸ (grey line). (C) Fluorescence recovery after photobleaching of GFP-actin in the cortex of HeLa cells blocked in prometaphase. Solid lines indicate fluorescence recovery after photobleaching and are the average of $N=10$ measurements on $n=4$ cells.

Figure S9

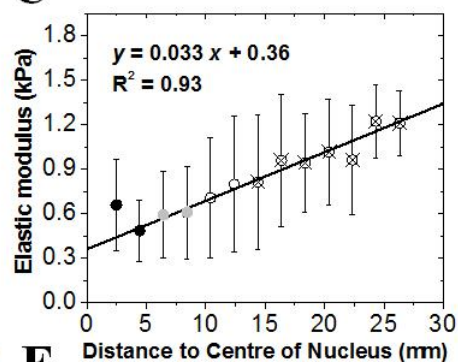
A



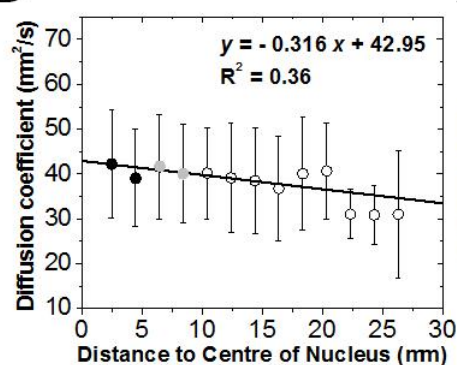
B



C



D



E

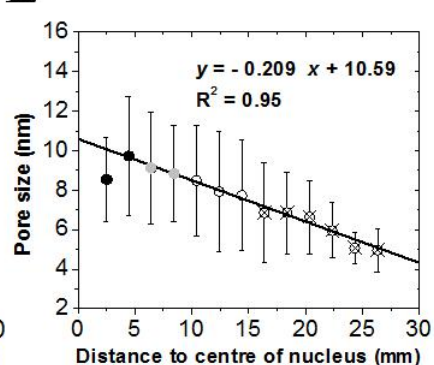
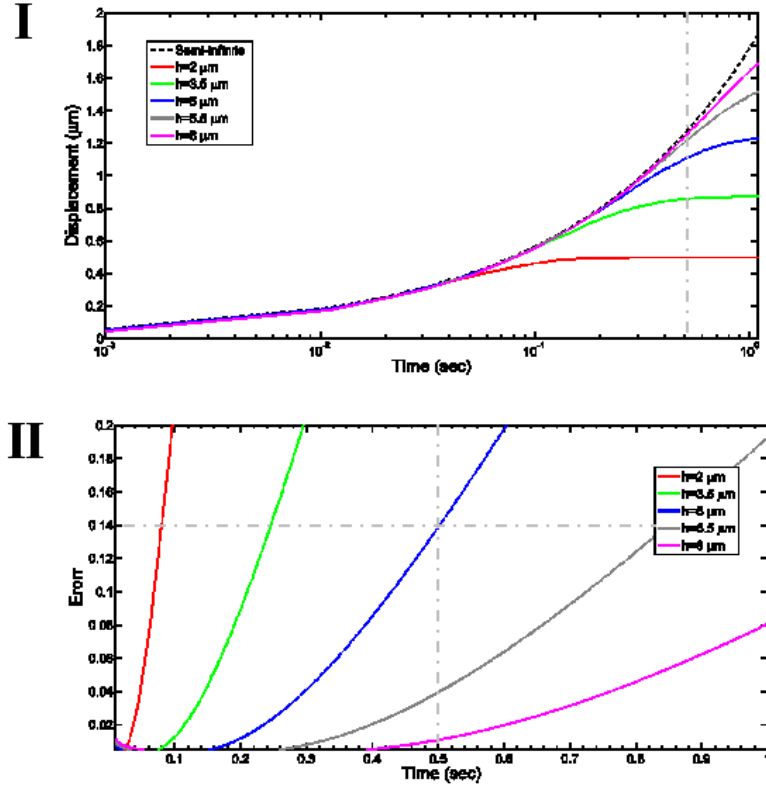


FIGURE S9 Spatial distribution of cellular rheological properties. (A) Representative phase contrast image of a HeLa cell and the location of AFM measurements on its surface (I). The position of the height reference, where the AFM tip contacts the glass surface was also chosen as the xy reference (fluorescence image of the bead, IV). The location of the nucleus was determined using Hoechst 34332 staining (III) and the centroid of the nucleus was used as a reference for displaying data. To determine the exact pathline of the bead and to calculate the distance of each point from the centre of nucleus, images of the cell (II), the cell nucleus (III), and the bead (IV) were overlaid (I). Scale bars =10 μm . (B-E) Scatter plots of the average cell height, poroelastic diffusion constant, elasticity, and lumped pore size as a function of distance to the centre of nucleus. Each scatter graph is generated by averaging values of each variable over 2 μm wide bins. Filled black circles indicate locations above the nucleus, white open circles in the cytoplasm, and grey filled circles boundary areas. The lines indicate the weighted least-square fit of the scattered data. Open circles with a cross superimposed indicate measurements significantly different ($p<0.01$) from those obtained above the nucleus.

Figure S10

A



B

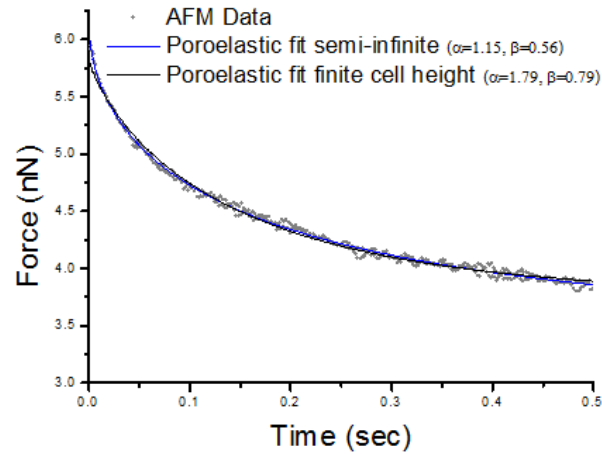


FIGURE S10 (A) (I) Settlement response of a surface after sudden application of $\sigma_{ave} = 250$ Pa for a poroelastic material with $E = 1$ kPa, $\nu_s = 0.5$ and $D_p = 40 \mu\text{m}^2 \cdot \text{s}^{-1}$. The dashed line is the infinite half-space response and the coloured lines correspond to the solutions for poroelastic materials with thicknesses ranging from $h = 2$ to $8 \mu\text{m}$. (II) Normalised difference between the infinite half-space solution and the finite thickness solution for different times after stress application. (B) Experimental force-relaxation data (grey dots) fitted with empirical solutions for force-relaxation of poroelastic materials assuming the cell has a finite height (black) or that the cell can be approximated as a semi-infinite half-plane (blue). Both empirical solutions fitted the experimental data well.